

SYNCHROTRON SELF-COMPTON AS A LIKELY MECHANISM OF  
PHOTONS BEYOND THE SYNCHROTRON LIMIT IN GRB 190114CN. FRAIJA<sup>1†</sup>, R. BARNIOL DURAN<sup>2</sup>, S. DICHARA<sup>3,4</sup> AND P. BENIAMINI<sup>5</sup><sup>1</sup>Instituto de Astronomía, Universidad Nacional Autónoma de México, Apdo. Postal 70-264, Cd. Universitaria, México DF 04510<sup>2</sup>Department of Physics and Astronomy, California State University, Sacramento, 6000 J Street, Sacramento, CA 95819-6041, USA<sup>3</sup>Department of Astronomy, University of Maryland, College Park, MD 20742-4111, USA<sup>4</sup>Astrophysics Science Division, NASA Goddard Space Flight Center, 8800 Greenbelt Rd, Greenbelt, MD 20771, USA<sup>5</sup>Department of Physics, The George Washington University, Washington, DC 20052, USA*Draft version September 4, 2019*

## ABSTRACT

GRB 190114C, a long and luminous burst, was detected by several satellites and ground-based telescopes from radio wavelengths to GeV gamma-rays. In the GeV gamma-rays, the Fermi LAT detected 48 photons above 1 GeV during the first hundred seconds after the trigger time, and the MAGIC telescopes observed for more than one thousand seconds very-high-energy (VHE) emission above 300 GeV. Previous analysis of the multi-wavelength observations showed that although these are consistent with the synchrotron forward-shock model that evolves from a stratified stellar-wind to homogeneous ISM-like medium, photons above few GeVs can hardly be interpreted in the synchrotron framework. In the context of the synchrotron forward-shock model, we derive the light curves and spectra of the synchrotron self-Compton (SSC) model in the stratified and homogeneous medium. In particular, we study the evolution of these light curves during the stratified-to-homogeneous afterglow transition. Using the best-fit parameters reported for GRB 190114C we interpret the photons beyond the synchrotron limit in the SSC framework and model its spectral energy distribution. We conclude that low-redshift GRBs described under a favourable set of parameters as found in the early afterglow of GRB 190114C could be detected at hundreds of GeVs, and also afterglow transitions would allow that VHE emission could be observed for longer periods.

*Subject headings:* Gamma-rays bursts: individual (GRB 190114C) — Physical data and processes: acceleration of particles — Physical data and processes: radiation mechanism: nonthermal — ISM: general - magnetic fields

## 1. INTRODUCTION

Gamma-ray bursts (GRBs) are the most luminous explosions in the Universe, and one of the most promising sources for multimessenger observation of non-electromagnetic signals such as very-high-energy (VHE) neutrinos, cosmic rays and gravitational waves. Observation of sub-TeV photons from bursts would provide crucial information of GRB physics including hadronic and/or leptonic contributions, values of the bulk Lorentz factors as well as microphysical parameters. In the Fermi Large Area Telescope (LAT) era, detections of bursts linked to GeV photons have been pivotal in painting a comprehensive picture of GRBs.

Recently, Ajello et al. (2019) reported the second Fermi-LAT catalog which summarized the temporal and spectral properties of the 169 GRBs with high-energy photons above 100 MeV detected from 2008 to 2018. Among the highest energy photons associated (with high probability  $> 0.9$ ) with these bursts are: a 31.31-GeV photon arriving at 0.83 s after the trigger, a 33.39 GeV-photon at 81.75 s and a 19.56-GeV photon at 24.83 s, which were located around GRB 090510, GRB 090902B and GRB 090926A, respectively. Beside this list, GRB 130427A presented the highest energy photons ever detected, 73 GeV and 95 GeV observed at 19 s and 244 s, respectively (Ackermann et al. 2014), and GRB 160509A was related to a 52-GeV photon at 77 s after the trigger (Longo et al. 2016). These bursts exhibited two crucial similarities: i) The first high-energy photon ( $\geq 100$  MeV) was delayed with the onset of the prompt phase that was usually reported in the range of hundreds of keV and ii) The high-energy emission

was temporarily extended, with a duration much longer than the prompt emission which was typically less than  $\sim 30$  seconds.

In the range of GeV and harder, VHE emission is expected from the nearest and the brightest bursts. Alternative mechanisms to synchrotron radiation have been widely explored at internal as well as external shocks to interpret this emission. Using hadronic models, photo-hadronic interactions (Asano et al. 2009; Dermer et al. 2000; Fraija 2014) and inelastic proton-neutron collisions (Mészáros & Rees 2000) have been proposed. However, the non-temporal coincidence between GRBs and neutrinos reported by the IceCube collaboration have suggested that the amount of hadrons are low enough so that hadronic interactions are non efficient processes (Abbasi et al. 2012; Aartsen et al. 2016, 2015). Using leptonic models, external inverse Compton (EIC; Papathanassiou & Meszaros 1996; Panaitescu & Mészáros 2000; Fraija & Veres 2018) and synchrotron self-Compton (SSC; Zhang & Mészáros 2001; Veres & Mészáros 2012; Wang et al. 2001; Fraija et al. 2012; Sacahui et al. 2012; Fraija et al. 2019a,b,d,e,f) scenarios have been explored. Therefore, photons with energies higher than 5 - 10 GeV as detected before (Hurley et al. 1994) and during the Fermi LAT era (Abdo et al. 2009b; Ackermann et al. 2014, 2013, and therein) could be evidence of the inverse Compton (IC) scattering existence. Several authors have taken into account the two crucial similarities found in the Fermi LAT light curves and have concluded that VHE emission has its origin in external shocks (Kumar & Barniol Duran 2009, 2010; Ghisellini et al. 2010; Nava et al. 2014; Fraija et al. 2016b; Zou et al. 2009). In particular, Wang et al. (2013) showed that 10 - 100 GeV photons detected after

†nfraija@astro.unam.mx

the prompt phase could have originated by SSC emission of the early afterglow. In the context of external shocks and requiring observations in other wavelengths, several LAT-detected bursts have been described reaching similar conclusions (Liu et al. 2013; Beniamini et al. 2015; Fraija et al. 2016a).

For the first time, an excess of gamma-ray events with a significance of  $20\sigma$  during the first 20 minutes and photons with energies higher than 300 GeV was recently reported by the MAGIC collaboration from GRB 190114C (Mirzoyan 2019). This burst triggered the Burst Area Telescope (BAT) instrument onboard Swift satellite at 2019 January 14 20:57:06.012 UTC (trigger 883832) (Gropp 2019) and it was followed up by the Gamma-Ray Burst Monitor (GBM; Kocevski 2019), by LAT (Kocevski 2019), by the X-ray Telescope (XRT; Gropp 2019; Osborne 2019), by the Ultraviolet/Optical Telescope (UVOT; Gropp 2019; Siegel 2019), by the SPI-ACS instrument (Minaev & Pozanenko 2019), by the Mini-CALorimeter instrument (Ursi et al. 2019), by the Hard X-ray Modulation Telescope instrument (Xiao et al. 2019), by Konus-Wind (Frederiks et al. 2019), by the Atacama Large Millimeter/submillimeter Array (ALMA), by the Very Large Array (VLA) (Laskar et al. 2019) and by several optical telescopes (Tyurina 2019; Lipunov 2019; Selsing 2019; Izzo 2019; Mirzoyan 2019; Bolmer & Shady 2019; Im 2019a; Alexander 2019; D’Avanzo 2019; Im 2019b; Mazaeva 2019).

Ravasio et al. (2019) analyzed the GBM data and found a typical prompt emission for the first  $\sim 4$  s, a smoothly broken-power law spectrum. However, the GBM data for  $\gtrsim 4$  s showed that i) the spectral evolution was consistent with a single component similar to that of the LAT spectrum and ii) the time of the bright peak coincided with the peak exhibited in the LAT data. They concluded that both emissions were originated during the afterglow phase. Similarly, Wang et al. (2019b) analyzed the GBM and LAT data, finding that the MeV and GeV emission of GRB 190114C had the same origin during the afterglow evolution. Using the standard SSC model in a homogeneous medium, Wang et al. (2019a) described the broadband SED of GRB 190114C during the first 150 s after the trigger time. These authors concluded that the detection of the energetic photons at hundred of GeVs was due to the large burst energy and low redshift. Derishev & Piran (2019) argued that these photons were produced by the Comptonization of X-ray photons.

Fraija et al. (2019c) analyzed the gamma-ray (LAT and GBM), X-ray (BAT and XRT), optical (several telescopes) and radio (ALMA) light curves of GRB 190114C. These authors showed that the multi-wavelength observations during the first  $\sim 400$  s were consistent with the external shock model evolving in a stratified stellar-wind like medium and after this time were consistent with a uniform ISM-like medium. They also reported the external shock parameters they found using the Markov-chain Monte Carlo method when modelling the multi-wavelength (from radio to Fermi LAT) data. Moreover, these authors argued that the high-energy photons were produced in the deceleration phase and that an alternative mechanism originated in the forward shocks should be considered to properly describe the energetic photons with energies beyond the synchrotron limit. In particular, the specific model that transitions from stratified stellar-wind to an homogeneous interstellar medium was chosen because the synchrotron seed photons

for Comptonization can reproduce the multi-wavelength observations, and also the VHE photons detected for almost 20 minutes by the MAGIC telescope, which covered the time lapse before and after this transition. It is worth noting that before this transition, as suggested by some authors (e.g., see Ravasio et al. 2019; Wang et al. 2019b; Fraija et al. 2019c), the LAT, GBM, X-ray and optical observations are consistent with the evolution of the wind medium afterglow model, and after this transition the X-ray and optical observations with the constant medium afterglow model (e.g., see Wang et al. 2019a; Fraija et al. 2019c). Motivated by these results, we extend the results shown in Fraija et al. (2019c) and derive, in this paper, the SSC light curves and spectra in a stratified stellar-wind medium, which transitions to an homogeneous interstellar medium. The paper is organized as follows. In Section 2 we show SSC light curves generated in the forward shock when the outflow decelerates in a stratified stellar-wind and homogeneous ISM-like medium. In Section 3 we apply the SSC model to estimate the VHE emission of GRB 190114C using the parameters reported in Fraija et al. (2019c) and also discuss the results. In Section 4, conclusions are presented.

## 2. SSC SCENARIO OF FORWARD SHOCKS

It is widely accepted that the standard synchrotron forward-shock model has been successful in describing the multiwavelength (X-ray, optical and radio) observations in GRB afterglows. However, relativistic electrons are also expected to be cooled down by SSC emission (e.g. Sari & Esin 2001). We do not discuss the effects of the self-absorption frequency, since it is typically relevant at low energies compared to the GeV energy range (e.g., see Panaitescu et al. 2014). We do not use the reverse-shock emission because it was used in Fraija et al. (2019c) to explain the short-lasting Fermi LAT and GBM peaks at  $\sim 8$  s and it cannot describe an emission much longer than this timescale. Due to the absence of neutrinos spatially or temporally associated with GRB 190114C (Vandenbroucke 2019), we neglect more complex models like hadronic or photo-hadronic processes (Asano et al. 2009; Fraija 2014). They are by no means disfavored by these arguments. The SSC forward-shock model varies the temporal and spectral features of GRB afterglows significantly and can also explain the gamma-rays above the well-known synchrotron limit (e.g., Piran & Nakar 2010; Abdo et al. 2009a; Barniol Duran & Kumar 2011; Fraija et al. 2019c). The SSC emission of a decelerating outflow moving through either a stratified or homogeneous medium is calculated in the next section.

### 2.1. SSC light curves in the stratified stellar-wind medium

When the outflow interacts with the stratified medium with density  $\rho(r) = Ar^{-2}$ , where  $A = \frac{\dot{M}}{4\pi v_{\text{sw}}}$ ,<sup>1</sup> the minimum and the cooling electron Lorentz factors can be written as

$$\begin{aligned}\gamma_{\text{m}} &= 5.3 \times 10^2 g(p) \varepsilon_{e,-2} \Gamma_{2.5}, \\ \gamma_{\text{c}} &= 2.1 \times 10^5 \left( \frac{1 + Y_{\text{Th}}}{3} \right)^{-1} \xi^2 \varepsilon_{B,-4} A_{W,-1}^{-2} \Gamma_{2.5}^{-3} E_{53.5},\end{aligned}\quad (1)$$

respectively. Hereafter, we adopt the convention  $Q_{\text{x}} = Q/10^{\text{x}}$  in c.g.s. units. The microphysical parameters  $\varepsilon_{\text{B}}$

<sup>1</sup>  $\dot{M}$  is the mass-loss rate and  $v$  is the velocity of the outflow

and  $\epsilon_e$  correspond to the fraction of the shocked energy density transferred to the magnetic field and electrons, respectively, the equivalent kinetic energy  $E$  is associated with the isotropic energy  $E_{\gamma, \text{iso}}$  and the kinetic efficiency  $\eta = E_{\gamma, \text{iso}}/E$  which is defined as the fraction of the kinetic energy radiated into gamma-rays,  $Y_{\text{Th}}$  is the Compton parameter (Sari & Esin 2001; Wang et al. 2010),  $\xi$  is a constant parameter of order of unity (Chevalier & Li 2000),  $g(p) = \frac{p-2}{p-1} \simeq 0.23$  for  $p = 2.3$ ,  $\Gamma$  is the bulk Lorentz factor and  $A_W = A/(5 \times 10^{11} \text{ g cm}^{-1})$  is the parameter of wind density (Panaitescu & Kumar 2000; Vink et al. 2000; Vink & de Koter 2005; Chevalier et al. 2004; Dai & Lu 1998; Chevalier & Li 2000).

Given the hydrodynamic forward-shock evolution in the stratified medium  $\Gamma \sim 258.3 \left(\frac{1+z}{1.5}\right)^{\frac{1}{4}} E_{53.5}^{\frac{1}{4}} A_{W,-1}^{-\frac{1}{4}} t_2^{-\frac{1}{4}}$  and the photon energy radiated by synchrotron process  $\epsilon_\gamma(\gamma_e) \propto \Gamma B' \gamma_e^2$  with  $B'$  the comoving magnetic field, the synchrotron spectral breaks and the maximum flux evolve as  $\epsilon_{\text{m}}^{\text{syn}} \propto t^{-\frac{3}{2}}$ ,  $\epsilon_{\text{c}}^{\text{syn}} \propto t^{\frac{1}{2}}$  and  $F_{\text{max}}^{\text{syn}} \propto t^{-\frac{1}{2}}$ , respectively (Panaitescu & Kumar 2000).

Photons generated by synchrotron radiation can be up-scattered in the forward shocks by the same electron population as  $\epsilon_{\text{m(c)}}^{\text{ssc}} \sim \gamma_{\text{m(c)}}^2 \epsilon_{\text{m(c)}}^{\text{syn}}$  with a maximum flux given by  $F_{\text{max}}^{\text{ssc}} \sim k\tau F_{\text{max}}^{\text{syn}}$ , where  $\tau$  is the optical depth and  $k = \frac{4(p-1)}{p-2}$ . Therefore, taking into account the electron Lorentz factors (eq. 1) and the synchrotron spectral breaks (Chevalier & Li 2000), the SSC spectral breaks and the maximum flux for SSC emission can be written as

$$\begin{aligned} \epsilon_{\text{m}}^{\text{ssc}} &\simeq 15.1 \text{ keV} g(p)^4 \left(\frac{1+z}{1.5}\right) \xi^{\frac{1}{2}} \epsilon_{e,-2}^4 \epsilon_{B,-4}^{\frac{1}{2}} A_{W,-1}^{-\frac{1}{2}} E_{53.5} t_2^{-2}, \\ \epsilon_{\text{c}}^{\text{ssc}} &\simeq 97.5 \text{ TeV} \left(\frac{1+z}{1.5}\right)^{-3} \left(\frac{1+Y_{\text{Th}}}{3}\right)^{-4} \xi^{\frac{9}{2}} \epsilon_{B,-4}^{-\frac{7}{2}} A_{W,-1}^{-\frac{9}{2}} \\ &\quad \times E_{53.5} t_2^2, \\ F_{\text{max}}^{\text{ssc}} &\simeq 1.1 \times 10^{-4} \text{ mJy} \left(\frac{1+z}{1.5}\right)^2 \xi^{-\frac{5}{2}} \epsilon_{B,-4}^{\frac{1}{2}} A_W^{\frac{5}{2}} D_{27}^{-2} t_2^{-1}, \quad (2) \end{aligned}$$

where  $z = 0.5$  is the redshift and  $D$  is the luminosity distance of the burst. The luminosity distance is obtained using the values of cosmological parameters reported in Planck Collaboration et al. (2018): the matter density parameter of  $\Omega_{\text{m}} = 0.315 \pm 0.007$  and the Hubble constant of  $H_0 = 67.4 \pm 0.5 \text{ km s}^{-1} \text{ Mpc}^{-1}$ .

During the deceleration phase the intrinsic attenuation by  $e^\pm$  pair production due to collision of a VHE photon with a lower-energy photon is given by (e.g., see Vedrenne & Atteia 2009)

$$\tau_{\gamma\gamma, \text{in}} \simeq 10^{-2} R_{\text{dec}, 17} \Gamma_{2.5}^{-1} n_{\gamma, 10.8}, \quad (3)$$

where  $R_{\text{dec}} = 1.17 \times 10^{17} \text{ cm} \left(\frac{1+z}{1.5}\right)^{\frac{1}{2}} \xi A_{-1}^{-\frac{1}{2}} E_{53.5}^{\frac{1}{2}} t_2^{\frac{1}{2}}$  is the deceleration radius and  $n_{\gamma} \simeq 6 \times 10^{10} \text{ cm}^{-3} L_{\gamma, 50}^{-2} R_{\text{dec}, 17}^{-1} \Gamma_{2.5}^{-1} \epsilon_{\gamma, 3}^{-1}$  is the keV-photon density ( $\epsilon_{\gamma, 3} = 1 \text{ keV}$ ) with  $L_{\gamma}$  the keV-photon luminosity. Since  $\tau_{\gamma\gamma, \text{in}} \ll 1$  during the deceleration phase, the intrinsic attenuation (opacity) is not considered.

Given the SSC spectra for fast- and slow-cooling regime together with the SSC spectral breaks and the maximum flux (eq. 2), the SSC light curves in the fast (slow)-cooling regime are

$$F_{\nu}^{\text{ssc}} = \begin{cases} F_{1, \text{f(s)}}^W t_2^{-\frac{5}{3}} (t_2^{-\frac{1}{3}}) \epsilon_{\gamma, 11}^{\frac{1}{3}}, & \epsilon_\gamma < \epsilon_{\text{c}}^{\text{ssc}}(\epsilon_{\text{m}}^{\text{ssc}}), \\ F_{2, \text{f(s)}}^W t_2^0 \epsilon_{\gamma, 11}^{-\frac{1}{2}} (t_2^{-p} \epsilon_{\gamma, 11}^{-\frac{p-1}{2}}), & \epsilon_{\text{c}}^{\text{ssc}}(\epsilon_{\text{m}}^{\text{ssc}}) < \epsilon_\gamma < \epsilon_{\text{m}}^{\text{ssc}}(\epsilon_{\text{c}}^{\text{ssc}}), \\ F_{3, \text{f(s)}}^W t_2^{1-p} \epsilon_{\gamma, 11}^{-\frac{p}{2}}, & \{\epsilon_{\text{m}}^{\text{ssc}}, \epsilon_{\text{c}}^{\text{ssc}}\} < \epsilon_\gamma, \end{cases} \quad (4)$$

where  $\epsilon_{\gamma, 11} = 100 \text{ GeV}$  and  $t_2 = 100 \text{ s}$  correspond to the energy band and timescale at which the flux is estimated. The values of the proportionality constants  $F_{\text{m,n}}^W$  for  $m = 1, 2$  and  $3$  and  $n = \text{f (fast) or s (slow)}$  are reported in appendix A. The SSC light curves agree with the ones derived in Panaitescu & Kumar (2000) for a stratified medium. It is worth noting that these authors calculated the light curves for the energy band of X-rays and timescales of days.

In the SSC spectrum, the Klein-Nishina (KN) regime must be considered because the emissivity beyond this frequency is drastically decreased compared with the classical Thomson regime. The spectral break caused by the decrease of the scattering cross section, due to the KN effects, is given by

$$\epsilon_{\text{KN}}^{\text{ssc}} \simeq 8.8 \text{ TeV} \left(\frac{1+z}{1.5}\right)^{-\frac{3}{2}} \left(\frac{1+Y_{\text{Th}}}{3}\right)^{-1} \xi^2 \epsilon_{B,-4}^{-1} A_{W,-1}^{-\frac{3}{2}} \times E_{53.5}^{\frac{1}{2}} t_2^{\frac{1}{2}}. \quad (5)$$

The SSC light curves given in eq. (4) show two features: i) The second PL segment of the fast-cooling regime ( $\epsilon_{\text{c}}^{\text{ssc}} < \epsilon_\gamma < \epsilon_{\text{m}}^{\text{ssc}}$ ) does not evolve with time, and others decrease gradually. It indicates that SSC emission is more likely to be detected during the first seconds after the trigger time, and ii) The first PL segment in the fast-cooling regime ( $\epsilon_\gamma < \epsilon_{\text{c}}^{\text{ssc}}$ ), and the third PL segments ( $\{\epsilon_{\text{m}}^{\text{ssc}}, \epsilon_{\text{c}}^{\text{ssc}}\} < \epsilon_\gamma$ ) are decaying functions of the circumburst density. It suggests that depending on the timescale and energy range observed, the SSC emission could be detected in environments with higher and/or lower densities.

The top panels in Figure 1 show the resulting light curves and SEDs of the SSC forward-shock emission generated by a decelerating outflow in a stratified medium. These panels were obtained using relevant values for GRB afterglows.<sup>2</sup> The observable quantities, the microphysical parameters, the parameter density and the efficiencies are in the range proposed to produce GeV photons in the afterglow phase (e.g., see Beniamini et al. 2015, 2016). The effect of the extragalactic background light (EBL) absorption proposed by Franceschini & Rodighiero (2017) was used. The gold and blue solid curves in the left-hand panel correspond to 10 and 100 GeV, respectively, and the gold and blue dashed-dotted curves to the Fermi LAT (Piron 2016) and the MAGIC (Takahashi et al. 2008) sensitivities at the same energies, respectively. The purple and green curves in the top right-hand panel correspond to the SEDs at 10 and 100 s, respectively.

The top panels show that the SSC flux is very sensitive to the external density. The light curves above the LAT and MAGIC sensitivities are obtained with  $A_W = 10^{-1}$  and below with  $A_W = 10^{-3}$ . In this particular case, both light curves (at 10 and 100 GeV) evolve in the second PL segment of slow-cooling regime. The spectral breaks are  $\epsilon_{\text{m}}^{\text{ssc}} = 0.5 \text{ MeV}$  and  $\epsilon_{\text{c}}^{\text{ssc}} = 2.8 \times 10^8 \text{ TeV}$  for  $A_W = 10^{-3}$ , and  $\epsilon_{\text{m}}^{\text{ssc}} = 47.5 \text{ keV}$  and  $\epsilon_{\text{c}}^{\text{ssc}} = 0.2 \text{ TeV}$  for  $A_W = 0.1$ . The transition times between fast to slow cooling regime are 0.03 and 0.3 s for  $A_W = 10^{-3}$  and 0.1, respectively. It shows that with these parameters the SSC emission decreases monotonically with time and increases as the density of the circumburst medium increases. For the chosen parameters, the break energies in the KN regime are  $1.2 \times 10^3 \text{ TeV}$  and  $1.3 \text{ TeV}$  for  $A_W = 10^{-3}$  and 0.1, respectively, which are above the energies of the Fermi and MAGIC sensitivities. We emphasize that depending on the parameter values, the SSC emission would lie in the KN regime, and then this emission would be drastically suppressed. Similarly, the electron distribution that up-scatters synchrotron forward-shock photons beyond the KN regime

<sup>2</sup>  $E = 5 \times 10^{53} \text{ erg}$ ,  $p = 2.3$ ,  $\epsilon_B = 10^{-3}$ ,  $\epsilon_e = 10^{-2}$ ,  $z = 0.5$ ,  $\xi = 1$  and  $A_W = 10^{-3}$  ( $10^{-1}$ ) for the purple (green) curve.



would be affected (Nakar et al. 2009; Wang et al. 2010) and also the degree of cooling of synchrotron emitting electrons would be affected by KN (Beniamini et al. 2015).

The top left-hand panel of Fig. 1 shows that the SSC flux is above the Fermi LAT and MAGIC sensitivities during the first 100 s for  $A_W = 0.1$  but not for the value of  $A_W = 10^{-3}$ . Therefore, the probability to observe the SSC emission from the GRB afterglow is higher during the first seconds after the burst trigger than at late times, and when the stellar wind ejected by the progenitor is denser.

The top right-hand panel shows the SEDs for the same set of parameters at  $t = 10$  and 100 s. The value of  $A_W = 0.1$  corresponds to the curve above the Fermi LAT and MAGIC sensitivities and the value of  $A_W = 10^{-3}$  to the curve below the sensitivities. The red dashed line corresponds to the maximum energy radiated by synchrotron. The filled areas in gray and cyan colors correspond to the Fermi LAT and MAGIC energy ranges, respectively. The Fermi LAT and MAGIC areas show that photons above the synchrotron limit can be explained by SSC emission. In addition, the top right-hand panel displays that the maximum SSC flux, due to EBL absorption, lies at i) the end of the LAT energy range where this instrument has less sensitivity (Funk & Hinton 2013) and ii) the beginning of the MAGIC energy range, making this telescope ideal for detecting the SSC emission.

In order to compare the synchrotron and SSC fluxes at Fermi LAT energies (e.g.  $\epsilon_\gamma = 800$  MeV), we obtain the synchrotron and SSC spectral breaks at  $t = 10^2$  s for  $A_W = 0.1$  ( $\epsilon_m^{\text{syn}} = 0.2$  eV,  $\epsilon_c^{\text{syn}} = 0.3$  keV,  $\epsilon_m^{\text{SSC}} = 47.5$  keV,  $\epsilon_c^{\text{SSC}} = 0.2$  TeV). Therefore, at the Fermi LAT energy range the synchrotron emission evolves in the third PL segment of slow-cooling regime and SSC emission in the second PL segment. In this case, the ratio of synchrotron and SSC fluxes becomes

$$\frac{F_\nu^{\text{syn}}}{F_\nu^{\text{SSC}}} \sim 1.6 \left( \frac{1+z}{1.5} \right)^{\frac{1}{4}} \xi^{\frac{7}{2}} \left( \frac{1+Y_{\text{Th}}}{2} \right)^{-1} \epsilon_{e,-2}^{-p+\frac{1}{4}} A_{W,-1}^{-\frac{5}{2}} E_{53.5}^{\frac{3}{4}} \Gamma_{2.5}^{1-p} t_2^{\frac{3}{2}} \left( \frac{\epsilon_\gamma}{800 \text{ MeV}} \right)^{-\frac{1}{2}}, \quad (6)$$

which is of order unity. Here, we use a smaller value of the effective Compton Y parameter because electrons radiating synchrotron at these large energies have a Compton Y parameter smaller than the corresponding value in the Thomson regime.

<sup>3</sup> We can conclude that below  $\sim 300$  MeV the flux can be described in the synchrotron forward-shock scenario, between  $\sim 0.5 - 1$  GeV the contribution of both processes would be relevant, and beyond the synchrotron limit, the observations would be entirely explained by SSC process for this set of parameters.

The top right-hand panel shows that the maximum SSC flux lies at 100 GeV, making it possible to detect the VHE emission in observatories where the sensitivity is maximum at hundreds of GeV (e.g. MAGIC telescope) but not in those observatories where the maximum sensitivity lies in few TeVs (e.g. High Altitude Water Cherenkov (HAWC); Abeysekara

<sup>3</sup> The energy break of scattering photons above which the scatterings with the electron population given by Lorentz factor  $\gamma_e$  lie the KN regime is given by  $\epsilon_{\text{KN}}^{\text{syn}}(\gamma_e) = m_e c^2 \frac{\Gamma}{\gamma_e}$  (Wang et al. 2010; Beniamini et al. 2015). For

$\gamma_e = \gamma_c$ , eqs. 1 and 5 are related by  $\epsilon_{\text{KN}}^{\text{syn}}(\gamma_c) = \frac{\epsilon_{\text{KN}}^{\text{SSC}}}{\gamma_c^2} \simeq 2.1$  keV. Taking into account that the electron Lorentz factor of  $\gamma_e^* \simeq 3 \times 10^7$  produces the synchrotron photons at  $\sim 300$  MeV, the corresponding KN photon energy is  $\epsilon_{\text{KN}}^{\text{syn}}(\gamma_e^*) \simeq 1.4$  eV. Given that the characteristic and cutoff synchrotron breaks are  $\epsilon_m^{\text{syn}} = 1.6$  eV and  $\epsilon_c^{\text{syn}} = 0.2$  keV, respectively, the Compton parameter lies in the range  $\epsilon_{\text{KN}}^{\text{syn}}(\gamma_e^*) < \epsilon_m^{\text{syn}} < \epsilon_c^{\text{syn}} < \epsilon_{\text{KN}}^{\text{syn}}(\gamma_c)$ . For

this case,  $Y(\gamma_e^*) = Y_{\text{Th}} \left( \frac{\epsilon_m^{\text{syn}}}{\epsilon_c^{\text{syn}}} \right)^{\frac{3-p}{2}} \left( \frac{\epsilon_{\text{KN}}^{\text{syn}}(\gamma_e^*)}{\epsilon_m^{\text{syn}}} \right)^{\frac{1}{4}} \simeq 0.57 Y_{\text{Th}}$  with  $Y_{\text{Th}} = 1.93$ .

& et al. 2012). For instance, the SSC flux at 1 TeV decreases between two and three orders of magnitude in comparison with the flux at 100 GeV.

Given the minimum and cooling electron Lorentz factors (eq. 1), the synchrotron and SSC luminosity ratio can be computed as <sup>4</sup>

$$\frac{L_\nu^{\text{SSC}}}{L_\nu^{\text{syn}}} \simeq 0.41 A_{W,-1} R_{\text{dec},17}^{-1} \gamma_{c,5}^2 \left( \frac{\gamma_{c,5}}{\gamma_{m,2}} \right)^{1-p}. \quad (7)$$

It is worth mentioning that the synchrotron and SSC luminosity ratio depends on Y through  $\gamma_c$ . Therefore, in the case of a stratified medium, half of the synchrotron luminosity is up-scattered by SSC emission.

## 2.2. SSC light curves in a homogeneous ISM-like medium

When the outflow interacts with a homogeneous medium with density  $n$ , the minimum and the cooling electron Lorentz factors can be written as

$$\gamma_m = 4.3 \times 10^2 g(p) \epsilon_e \Gamma_2, \\ \gamma_c = 1.9 \times 10^4 \left( \frac{1+Y_{\text{Th}}}{1.5} \right)^{-1} \left( \frac{1+z}{2.5} \right) \epsilon_{B,-4}^{-1} n^{-1} \Gamma_2^{-3} t_3^{-1}. \quad (8)$$

Given the hydrodynamic forward-shock evolution in the homogeneous medium  $\Gamma \sim 101.2 \left( \frac{1+z}{1.5} \right)^{\frac{3}{8}} E_{53.5}^{\frac{1}{8}} n^{-\frac{1}{8}} t_3^{-\frac{3}{8}}$  and the photon energy radiated by synchrotron  $\epsilon_\gamma(\gamma_e) \propto \Gamma B' \gamma_e^2$ , the synchrotron spectral breaks and the maximum flux evolve as  $\epsilon_m^{\text{syn}} \propto t^{-\frac{3}{2}}$ ,  $\epsilon_c^{\text{syn}} \propto t^{-\frac{1}{2}}$  and  $F_{\text{max}}^{\text{syn}} \propto t^0$  (e.g., Sari et al. 1998).

Taking into consideration the electron Lorentz factors (eq. 8) and the synchrotron spectral breaks (Sari et al. 1998), the spectral breaks and the maximum flux for SSC emission can be written as

$$\epsilon_m^{\text{SSC}} \simeq 11.4 \text{ keV } g(p)^4 \left( \frac{1+z}{1.5} \right)^{\frac{5}{4}} \epsilon_{e,-2}^4 \epsilon_{B,-4}^{\frac{1}{2}} n^{-\frac{1}{4}} E_{53.5}^{\frac{3}{4}} t_3^{-\frac{9}{4}}, \\ \epsilon_c^{\text{SSC}} \simeq 0.1 \text{ TeV } \left( \frac{1+z}{1.5} \right)^{-\frac{3}{4}} \left( \frac{1+Y_{\text{Th}}}{2.5} \right)^{-4} \epsilon_{B,-4}^{-\frac{7}{2}} n^{-\frac{9}{4}} E_{53.5}^{-\frac{5}{4}}, \\ \times t_3^{-\frac{1}{4}}, \\ F_{\text{max}}^{\text{SSC}} \simeq 1.1 \times 10^{-5} \text{ mJy } \left( \frac{1+z}{1.5} \right)^{\frac{3}{4}} \epsilon_{B,-4}^{\frac{1}{2}} n^{\frac{5}{4}} D_{27}^{-2} E_{53.5}^{\frac{5}{4}} t_3^{\frac{1}{4}}. \quad (9)$$

Given the synchrotron spectra for fast- and slow-cooling regime together with the SSC spectral breaks and the maximum flux (eq. 9), the SSC light curves in the fast (slow)-cooling regime are (Sari & Esin 2001)

$$F_\nu^{\text{SSC}} = \begin{cases} F_{1,f(s)}^H t_3^{\frac{1}{3}} (t_3)^{\frac{1}{3}} \epsilon_{\gamma,11}^{\frac{1}{3}}, & \epsilon_\gamma < \epsilon_c^{\text{SSC}}(\epsilon_m^{\text{SSC}}), \\ F_{2,f(s)}^H t_3^{\frac{1}{3}} \epsilon_{\gamma,11}^{\frac{1}{3}} (t_3)^{-\frac{1}{2}} (t_3)^{-\frac{9p-11}{8}} \epsilon_{\gamma,11}^{-\frac{p-1}{2}}, & \epsilon_{\gamma,c}^{\text{SSC}}(\epsilon_m^{\text{SSC}}) < \epsilon_\gamma < \epsilon_m^{\text{SSC}}(\epsilon_c^{\text{SSC}}), \\ F_{3,f(s)}^H t_3^{-\frac{9p-10}{8}} \epsilon_{\gamma,11}^{-\frac{p}{2}}, & \{\epsilon_c^{\text{SSC}}, \epsilon_m^{\text{SSC}}\} < \epsilon_\gamma, \end{cases} \quad (10)$$

where  $\epsilon_{\gamma,11} = 100$  GeV and  $t_3 = 1000$  s correspond to the energy band and timescale at which the flux is estimated. The values of the proportionality constants  $F_{m,n}^H$  for  $m = 1, 2$  and  $3$  and  $n = f$  (fast) or  $s$  (slow) are reported in appendix A. It is worth noting that the time evolution of each PL segment of the SSC light curve agrees with the ones derived in Panaitescu & Kumar (2000) for the fast- and slow-cooling regime and the PL segments in the slow-cooling regime derived by Sari &

<sup>4</sup> This relation was obtained using the synchrotron and SSC luminosity ratio derived in Sari & Esin (2001) with the equivalent density for the stratified medium.

Esin (2001).

For the case of the homogeneous medium, the spectral break caused by the decrease of the scattering cross section, due to the KN effects, is given by

$$\epsilon_c^{\text{KN}} \simeq 0.7 \text{ GeV} \left( \frac{1+z}{1.5} \right)^{-\frac{3}{4}} \left( \frac{1+Y_{\text{Th}}}{2.5} \right)^{-1} \varepsilon_{B,-4}^{-1} n^{-\frac{3}{4}} E_{53.5}^{-\frac{1}{4}} \times t_3^{-\frac{1}{4}}. \quad (11)$$

The light curves given in eq. (10) show two important features: i) They show that at lower energies the SSC flux increases with time and at higher energies it decreases in both regimes (fast and slow). Therefore, it indicates that SSC emission is more probable to be detected during the first seconds after the trigger time, although if this emission is very strong it can be observed for long times. It is worth highlighting that the SSC emission at lower energies is eclipsed by the synchrotron radiation, and ii) The first PL segment in the fast-cooling regime ( $\epsilon_\gamma < \epsilon_c^{\text{SSC}}$ ), and the third PL segments ( $\{\epsilon_c^{\text{SSC}}, \epsilon_m^{\text{SSC}}\} < \epsilon_\gamma$ ) are decaying functions of the circumburst density. It suggests that depending on the timescale and energy range observed, the SSC emission could be detected in environments with higher and/or lower densities.

The bottom panels in Figure 1 show the resulting light curves and SEDs of the SSC forward-shock emission generated by a decelerating outflow in a homogeneous medium. These panels were obtained using relevant values for GRB afterglows.<sup>5</sup> The observable quantities, the microphysical parameters, the circumburst density and the efficiencies for a homogeneous density are in the range proposed to produce GeV photons in the afterglow phase (e.g. see, Beniamini et al. 2015, 2016). Again, the effect of the EBL absorption proposed by Franceschini & Rodighiero (2017) was considered. The bottom left-hand panel shows that the SSC flux is above the Fermi LAT and MAGIC sensitivities during the first 100 s for  $n = 0.1 \text{ cm}^{-3}$  but not for the value of  $n = 10^{-3} \text{ cm}^{-3}$ . The gold and blue solid curves in the top left-hand panel correspond to 10 and 100 GeV, respectively, and the gold and blue dashed-dotted curves to the Fermi LAT (Piron 2016) and the MAGIC (Takahashi et al. 2008) sensitivities at the same energies, respectively. The purple and green curves in the right-hand panel correspond to the SEDs at 10 and 100 s, respectively.

The bottom panels of Fig. 1 show that the SSC flux is very sensitive to the external density. The light curves above the LAT and MAGIC sensitivities are obtained with  $n = 10^{-1} \text{ cm}^{-3}$  and below with  $n = 10^{-3} \text{ cm}^{-3}$ . In this particular case, both light curves (at 10 and 100 GeV) evolve in the second PL segment of slow-cooling regime. The spectral breaks are  $\epsilon_m^{\text{SSC}} = 36.1 \text{ keV}$  and  $\epsilon_c^{\text{SSC}} = 5.3 \times 10^3 \text{ TeV}$  for  $n = 10^{-3} \text{ cm}^{-3}$ , and  $\epsilon_m^{\text{SSC}} = 11.4 \text{ keV}$  and  $\epsilon_c^{\text{SSC}} = 0.2 \text{ TeV}$  for  $n = 0.1 \text{ cm}^{-3}$ , respectively. The transition times between fast- to slow-cooling regime are 0.06 and 0.6 s for  $n = 10^{-3} \text{ cm}^{-3}$  and  $0.1 \text{ cm}^{-3}$ , respectively. It shows that with the chosen values the SSC emission decreases monotonically with time and increases as the density of the circumburst medium increases. Using the parameter values, the break energies in the KN regime are 31.7 TeV and 1.1 TeV for  $n = 10^{-3}$  and  $0.1 \text{ cm}^{-3}$ , respectively, which are above the energies of the Fermi and MAGIC sensitivities. Again, we emphasize that depending on the parameter values, the SSC emission would lie in the KN regime, and then this will be drastically suppressed. Similarly, the electrons population that up-scatters synchrotron photons beyond the KN regime would be altered (Nakar et al. 2009; Wang et al. 2010).

<sup>5</sup>  $E = 5 \times 10^{53} \text{ erg}$ ,  $p = 2.3$ ,  $\varepsilon_B = 10^{-3}$ ,  $\varepsilon_e = 10^{-2}$ ,  $z = 0.5$  and  $n = 10^{-3} (10^{-1}) \text{ cm}^{-3}$  for the purple (green) curve.

The bottom left-hand panel of Fig. 1 shows that the SSC flux at 10 GeV is above the Fermi LAT sensitivity after  $\sim 30$  s and at 100 GeV is above MAGIC sensitivity during the first 850 s for  $n = 0.1 \text{ cm}^{-3}$  but not for  $n = 10^{-3} \text{ cm}^{-3}$ . Therefore, the probability to detect the SSC emission from the GRB afterglow depends on the observed energy. For  $\epsilon_\gamma = 10 \text{ GeV}$ , the SSC emission could be detected delayed with respect to the prompt phase whereas for  $\epsilon_\gamma = 100 \text{ GeV}$  it could be detected in temporal coincidence with lower-energy photons.

The bottom right-hand panel of Fig. 1 shows the SEDs for the same parameter densities at  $t = 10^3$  and  $10^4$  s. The value of  $n = 0.1 \text{ cm}^{-3}$  corresponds to the curve above the Fermi LAT and MAGIC sensitivities and the value of  $n = 10^{-3} \text{ cm}^{-3}$  to the curve below these sensitivities. The red dashed line corresponds to the maximum energy radiated by synchrotron. The filled areas in gray and cyan colors correspond to the Fermi LAT and MAGIC energy ranges, respectively. The Fermi LAT and MAGIC areas show that photons above the synchrotron limit can be explained by SSC emission, similar to the case of the stratified medium. The maximum SSC flux, due to EBL absorption, lies at the lower end of the MAGIC energy range, making this telescope ideal for detecting the SSC emission generated in a homogeneous medium.

In order to compare the synchrotron and SSC fluxes at Fermi LAT energies (e.g.  $\epsilon_\gamma = 800 \text{ MeV}$ ), we obtain the synchrotron and SSC spectral breaks at  $t = 10^3$  s for  $n = 0.1 \text{ cm}^{-3}$  ( $\epsilon_\nu^{\text{syn}} = 6.1 \times 10^{-2} \text{ eV}$ ,  $\epsilon_c^{\text{syn}} = 0.3 \text{ keV}$ ,  $\epsilon_m^{\text{SSC}} = 11.4 \text{ keV}$ ,  $\epsilon_c^{\text{SSC}} = 0.2 \text{ TeV}$ ). Therefore, at the Fermi LAT energy range the synchrotron emission evolves in the third PL segment of slow-cooling regime and the SSC emission in the second PL segment. In this case, the ratio of synchrotron and SSC fluxes becomes

$$\frac{F_\nu^{\text{syn}}}{F_\nu^{\text{SSC}}} \sim 1.9 \left( \frac{1+z}{1.5} \right)^{-\frac{1}{4}} \left( \frac{1+Y_{\text{Th}}}{1.4} \right)^{-1} \varepsilon_{e,-2}^{1-p} \varepsilon_{B,-4}^{-\frac{3}{4}} n^{-\frac{7}{6}} E_{53.5}^{-\frac{1}{2}} \Gamma_{2.5}^{\frac{5}{2}-p} t_2^{-\frac{1}{4}} \left( \frac{\epsilon_\gamma}{800 \text{ MeV}} \right)^{-\frac{1}{2}}, \quad (12)$$

which is of order unity. We want to emphasize that the synchrotron and SSC flux ratio depends explicitly on  $Y$ . For the homogeneous medium, we use a smaller value of the effective Compton  $Y$  parameter because electrons radiating synchrotron at these large energies have a Compton  $Y$  parameter smaller than the corresponding value in the Thomson regime.

<sup>6</sup> We can conclude that below  $\sim 400 \text{ MeV}$  the observations can be described in the synchrotron forward-shock scenario, between  $\sim 0.6 - 1 \text{ GeV}$  the contribution of both processes would be relevant, and beyond the synchrotron limit, the observations would be entirely explained by SSC process for the set of values used.

The bottom right-hand panel of Fig. 1 shows that the maximum SSC flux lies at  $\sim 100 \text{ GeV}$ , making it possible to detect the VHE emission in observatories where the sensitivity is maximum at hundreds of GeV but not in those observatories where the maximum sensitivity lies in few TeVs (e.g. HAWC; Abeysekara & et al. 2012). Similar to the case of the stratified medium, the SSC flux at 1 TeV decreases between two and three orders of magnitude in comparison with the flux at 100 GeV.

<sup>6</sup> For the homogeneous medium, an analysis of the effective  $Y$  parameter for electrons radiating synchrotron at Fermi LAT energies can also be done. In this case, the break energies are  $\epsilon_{\text{KN}}(\gamma_e) = \frac{\epsilon_{\text{KN}}^{\text{KN}}}{\gamma_e^2} \simeq 0.9 \text{ keV}$ ,  $\epsilon_{\text{KN}}(\gamma_e^*) \simeq 0.6 \text{ eV}$ ,  $\epsilon_m^{\text{syn}} = 0.7 \text{ eV}$  and  $\epsilon_c^{\text{syn}} = 0.1 \text{ keV}$ . Again, the Compton parameter corresponding to the case  $\epsilon_{\text{KN}}(\gamma_e^*) < \epsilon_m^{\text{syn}} < \epsilon_c^{\text{syn}} < \epsilon_{\text{KN}}(\gamma_e)$  is  $Y(\gamma_e^*) \simeq 0.28 Y_{\text{Th}}$  with  $Y_{\text{Th}} = 1.45$ . Therefore, a similar conclusion to that found in the stratified case is given.

Given the minimum and cooling electron Lorentz factors (eq. 8), the synchrotron and SSC luminosity ratio can be computed as (Sari & Esin 2001)

$$\frac{L_{\nu}^{\text{SSC}}}{L_{\nu}^{\text{syn}}} \simeq 5.1 \times 10^{-2} n_{-1} R_{\text{dec},17}^2 \gamma_{c,4}^2 \left( \frac{\gamma_{c,4}}{\gamma_{m,2}} \right)^{1-p}, \quad (13)$$

where  $R_{\text{dec}} = 4.22 \times 10^{17} \text{ cm} \left( \frac{1+z}{1.5} \right)^{-\frac{1}{4}} n_{-1}^{-\frac{1}{4}} E_{53.5}^{\frac{1}{4}} t_3^{\frac{1}{4}}$  is the deceleration radius. Again, it is worth mentioning that the synchrotron and SSC luminosity ratio depends on  $Y$  through  $\gamma_c$ . In the case of the uniform medium, only 5% of the synchrotron luminosity is up-scattered by SSC emission.

### 2.3. The stratified-to-homogeneous afterglow transition

Figure 2 shows the SSC light curves and spectra during the afterglow transition between the stratified and homogeneous medium for typical values in the ranges:  $5 \times 10^{52} \leq E \leq 5 \times 10^{54} \text{ erg}$ ,  $0.1 \text{ cm}^{-3} \leq n \leq 1 \text{ cm}^{-3}$ ,  $10^{-2} \leq A_w \leq 1$ ,  $10^{-5} \leq \varepsilon_B \leq 10^{-3}$  and  $10^{-3} \leq \varepsilon_e \leq 10^{-1}$ . The top panels show the SSC light curves for  $\epsilon_\gamma = 100 \text{ GeV}$ . The stratified-to-homogeneous transition radius can be written as (e.g., see Fraija et al. 2017b)

$$R_{\text{tr}} \simeq 5.1 \times 10^{18} \text{ cm} \dot{M}_{-6}^{\frac{3}{10}} v_{W,8}^{\frac{1}{10}} n^{-\frac{3}{10}} t_{\star,5}^{\frac{2}{5}}, \quad (14)$$

where  $t_\star$  is the lifetime of the star phase for  $n = 1 \text{ cm}^{-3}$ . In our analysis, we have considered the stratified-to-homogeneous afterglow transition at 1000 s which correspond to a deceleration radius of  $\simeq 4.2 \times 10^{18} \text{ cm}$  for  $E = 5 \times 10^{54} \text{ erg}$  and  $A_w = 10^{-1}$  or  $E = 5 \times 10^{53} \text{ erg}$  and  $A_w = 10^{-2}$ . In the top left-hand panel, the light curves are computed for  $E = 5 \times 10^{53} \text{ erg}$ ,  $A_w = 1$  and  $n = 1 \text{ cm}^{-3}$  and in the top right-hand panel the light curves are obtained for  $\varepsilon_B = 10^{-4}$  and  $\varepsilon_e = 10^{-2}$ . These panels show that depending on the parameter values, the afterglow transition can be quite noticeable. For instance, in the purple curve there is actually a smoother transition (which is harder to detect) compared to some of the others. The top left-hand panel shows that SSC fluxes increase as  $\varepsilon_e$  increases in the stratified and the homogeneous medium; higher values of  $\varepsilon_e$  make SSC emission more favorable to be detected (indeed such values are expected to be common in GRB afterglows, see e.g., Santana et al. 2014; Beniamini & van der Horst 2017). Moreover, the SSC fluxes increase as  $\varepsilon_B$  decreases in the stratified but not in the homogeneous medium. The top right-hand panel shows that the SSC fluxes increase as  $E$ ,  $n$  and  $A_w$  increase in both the stratified and homogeneous medium.

The bottom panels of Fig. 2 show the SSC spectra computed in the stratified medium for  $t = 900 \text{ s}$  (left panel) and in the homogeneous medium for  $t = 1100 \text{ s}$  (right panel). The red dashed line represents the synchrotron limit. The bottom panels show that these spectra increase dramatically as  $\epsilon_e$  increases and slightly as  $\epsilon_B$  increases. The SSC light curves with the same colors (parameter values) represent the evolution from the stratified to homogeneous medium. As a consequence of this transition, one can observe that SSC fluxes increase up to more than one order of magnitude.

Figure 3 shows the synchrotron and SSC light curves, and the SEDs during the afterglow transition between the stratified and homogeneous medium. The spectrum and light curves of synchrotron emission have been included with the

purpose of performing a multi-wavelength analysis.

#### 2.3.1. Multi-wavelength Light Curves Analysis

The synchrotron light curves of optical and X-ray bands at 1 eV and 1 keV, and the SSC light curves of  $\gamma$ -rays at 100 GeV are shown in the top panels of Figure 3. In both panels it can be seen that while optical and X-ray fluxes display the same behavior,  $\gamma$ -rays exhibit a different one. For the given parameter values, during the afterglow transition the  $\gamma$ -ray flux can decrease (left panel) or increase (right panel). Taking into consideration the parameter values used in the top left-hand panel, for the stratified medium, the synchrotron and the SSC spectral breaks are  $\epsilon_m^{\text{syn}} = 5.1 \times 10^{-2} \text{ eV}$ ,  $\epsilon_c^{\text{syn}} = 2.3 \text{ keV}$ ,  $\epsilon_m^{\text{SSC}} = 15.1 \text{ keV}$ ,  $\epsilon_c^{\text{SSC}} = 97.7 \text{ TeV}$ ,  $\epsilon_c^{\text{KN}} = 8.8 \text{ TeV}$  and for the homogeneous medium, these breaks are  $\epsilon_m^{\text{syn}} = 2.2 \times 10^{-2} \text{ eV}$ ,  $\epsilon_c^{\text{syn}} = 1.8 \text{ keV}$ ,  $\epsilon_m^{\text{SSC}} = 3.6 \text{ keV}$ ,  $\epsilon_c^{\text{SSC}} = 8.3 \text{ TeV}$ ,  $\epsilon_c^{\text{KN}} = 2.4 \text{ TeV}$ . Considering the parameter values used in the right-hand panel, the SSC and synchrotron spectral breaks computed in the stratified medium are  $\epsilon_m^{\text{syn}} = 4.3 \text{ eV}$ ,  $\epsilon_c^{\text{syn}} = 3.5 \times 10^{-2} \text{ eV}$ ,  $\epsilon_m^{\text{SSC}} = 0.5 \text{ MeV}$ ,  $\epsilon_c^{\text{SSC}} = 0.5 \text{ keV}$ ,  $\epsilon_c^{\text{KN}} = 4.9 \text{ GeV}$  and these breaks computed in the homogeneous medium are  $\epsilon_m^{\text{syn}} = 8.5 \times 10^{-2} \text{ eV}$ ,  $\epsilon_c^{\text{syn}} = 14.3 \text{ eV}$ ,  $\epsilon_m^{\text{SSC}} = 10.8 \text{ keV}$ ,  $\epsilon_c^{\text{SSC}} = 0.2 \text{ GeV}$ ,  $\epsilon_c^{\text{KN}} = 2.6 \text{ GeV}$ . Therefore, from stratified-to-homogeneous medium the optical flux evolves in the second PL segment and the X-rays in the third PL segment of synchrotron model. During this transition phase the temporal index of the third PL segment of synchrotron emission ( $\propto t^{-\frac{3p-2}{4}}$ ) does not vary, and the second PL segment varies from  $\propto t^{-\frac{3p-1}{4}}$  to  $\propto t^{-\frac{3p-3}{4}}$ . However, an alternative interpretation different to the afterglow transition could be given in terms of the reverse-shock emission. In this framework, the X-rays are not altered and the optical flash is detected with a decay flux of  $\propto t^{-\frac{73p+21}{96}}$  and  $\propto t^{-\frac{27p+7}{35}}$  for the thick and thin shell, respectively (Kobayashi 2000). In this case, the analysis of the SSC light curve would be very useful in order to differentiate both interpretations. With the parameters given, the  $\gamma$ -ray evolves in the second PL segment close to the afterglow transition, from  $\propto t^{-p}$  to  $\propto t^{-\frac{1}{8}}$ . With the given parameters, the gamma-rays evolves in the second PL segment as the medium changes from wind to ISM from  $\propto t^{-p}$  or  $\propto t^{-\frac{1}{8}}$ , respectively; if the medium does not have this transition, then the flux would not show this particular break in the light curve. It is worth noting that while the afterglow transition is imperceptible for the synchrotron light curve at 1 keV, it presents a discontinuity quite evident for the SSC light curve at 100 GeV.

#### 2.3.2. The broadband Spectral Energy Distribution Analysis

The bottom panels of Fig. 3 show the SEDs computed in the stratified (left panel) and homogeneous (right panel) medium for a transition at 1000 s. For the case of stratified medium, we assume each SED at 100, 400 and 700 s and for the case of homogeneous medium, we calculate each SED at 1500, 3000 and 5000 s. Densities with values of  $A = 0.1$  and  $n = 1 \text{ cm}^{-3}$  are chosen for the stratified and homogeneous medium, respectively, and in both cases we use the same values  $E = 5 \times 10^{53} \text{ erg}$ ,  $\varepsilon_B = 10^{-4}$  and  $\varepsilon_e = 10^{-2}$  and  $\xi = 1.0$ . The principal features are: i) While the ratio between the maximum synchrotron and



the SSC fluxes decreases drastically in the stratified medium, it remains quasi-constant in the homogeneous medium. ii) While the synchrotron peak is shifted to higher energies as time increases in the stratified medium, it evolves quite slowly with time in the homogeneous medium. iii) While the maximum value of the SSC flux decreases quickly with time for the stratified medium, this value decreases gradually for the homogeneous medium. iv) An increase in the synchrotron and SSC fluxes is seen during the afterglow transition. At  $t = 700$  s the maximum values of synchrotron and SSC fluxes are  $3.5 \times 10^{-11}$  and  $4.2 \times 10^{-12}$  erg cm $^{-2}$  s $^{-1}$ , respectively, and at  $t = 1500$  s the maximum values of synchrotron and SSC fluxes are  $4.2 \times 10^{-11}$  and  $3.1 \times 10^{-11}$  erg cm $^{-2}$  s $^{-1}$  and iv) The evolution of the SED structures in both stratified and homogeneous medium are different. These characteristics could help identify if the transition phase exists or it is simply associated to a distinct scenario.

### 3. APPLICATION TO GRB 190114C

#### 3.1. Multi-wavelength Observations and previous analysis

GRB 190114C was triggered by the Burst Area Telescope (BAT) instrument onboard the Swift satellite on January 14, 2019 at 20:57:06.012 UTC (Gropp 2019). VHE photons with energies above 300 GeV were detected from this burst with a significance of  $20\sigma$  by the MAGIC telescope for more than 20 minutes (Mirzoyan 2019). GRB 190114C was followed up by a massive observational campaign with instruments onboard satellites and ground telescopes covering a large fraction of the electromagnetic spectrum (see Fraija et al. 2019c, and references therein). The host galaxy of GRB 190114C was located and confirmed to have a redshift of  $z = 0.42$  (Ugarte Postigo 2019; Selsing 2019). Recently, Fraija et al. (2019c) showed that the LAT light curve of GRB 190114C exhibited similar features to other bright LAT-detected bursts. Together with the multi-wavelength observations, the long-lived LAT, GBM, X-ray, optical and radio emissions were consistent with the standard synchrotron forward-shock model that evolves from a stratified to a homogeneous medium with an afterglow transition at  $\sim 400$  s. These authors showed that the high-energy photons were produced in the deceleration phase of the relativistic outflow and also that some additional processes to synchrotron in the forward shocks should be considered to properly describe the LAT photons with energies beyond the synchrotron limit. Here, we use the SSC process to interpret the photons beyond this synchrotron limit.

#### 3.2. Estimation of SSC light curves and VHE photons beyond the synchrotron limit

Using the best-fit values reported in Fraija et al. (2019c), the SSC light curves were calculated. The left-hand panel in Figure 4 shows the SSC light curves at 100 GeV in a stratified and homogeneous medium. This panel was adapted from Fraija et al. (2019c). The effect of the EBL absorption proposed by Franceschini & Rodighiero (2017) was included. The values of transition times between fast- and slow-cooling regime are 0.2 and 0.09 s for the stratified and homogeneous medium, respectively. The values of the characteristic and cutoff SSC breaks calculated in the stratified medium are  $\epsilon_m^{\text{SSC}} \simeq 0.2$  MeV and  $\epsilon_c^{\text{SSC}} \simeq 4.2 \times 10^4$  keV at 100 s, and in the homogeneous medium are  $\epsilon_m^{\text{SSC}} \simeq 1.6$  keV and  $\epsilon_c^{\text{SSC}} \simeq 1.6$  keV, respectively, at 1000 s. Therefore, in both cases the SSC light curves evolves in the second PL segment

of the slow-cooling regime. The break energies in the KN regime are 200.7 TeV and 868.1 GeV at 100 and  $10^3$  s, respectively. The highest energy photons reported by LAT and MAGIC collaboration are below the KN regime which agrees with the description of the SSC light curves. We emphasize that the parameters obtained with the MCMC code from the broadband modeling of the multi-wavelength observations may be changed somewhat when the KN effects are included, but the SSC emission itself will not be strongly affected. Therefore, VHE photons beyond the synchrotron limit can be explained through the second PL segment of the SSC emission in the slow-cooling regime.

In our model, the SSC emission decays steeper in the stratified than the homogeneous medium. However, during the stratified-to-homogeneous transition the SSC flux suddenly increases by  $\sim$  one order of magnitude. This allows that the SSC component could be detected during a longer time.

Abeysekara & et al. (2012) presented the HAWC sensitivity of the scaler system to GRBs for several declinations and energies (at which this observatory is sensitive). At 1 TeV and for a power-law index of  $p = 2.15 \pm 0.35$ , the HAWC sensitivities for the declinations of  $1.0 \geq \cos \theta > 0.9$ ,  $0.9 \geq \cos \theta > 0.8$ ,  $0.8 \geq \cos \theta > 0.7$  and  $0.7 \geq \cos \theta > 0.6$  are  $\sim (2.2 \times 10^{-7} - 1.1 \times 10^{-6})$  mJy,  $\sim (0.4 \times 10^{-6} - 2.5 \times 10^{-6})$  mJy,  $\sim (0.8 \times 10^{-6} - 0.7 \times 10^{-5})$  mJy and  $\sim (0.8 \times 10^{-5} - 0.7 \times 10^{-4})$  mJy, respectively. Taking into account the attenuation factor  $\sim 10^{-2}$  due to EBL at 1 TeV, the SSC flux would be  $\sim 10^{-10}$  mJy at  $10^2$  s and  $\sim 10^{-12}$  mJy at  $10^3$  s for the stratified and homogeneous medium, respectively. These values are well below the HAWC sensitivity for any declination. It shows that, with our model, GRB 190114C could not be detected by the HAWC observatory, even if this burst would have been located at the HAWC's field of view.

Funk et al. (2013) and Piron (2016) presented and discussed the sensitivity to transient sources as a function of duration of High Energy Stereoscopic System (HESS) CT5 and Cherenkov Telescope Array (CTA) telescopes for distinct energy thresholds. At 500 s, the HESS CT5 and CTA sensitivities for energy thresholds of 75 and 80 GeVs are  $\sim 2 \times 10^{-10}$  mJy and  $\sim 7 \times 10^{-10}$  mJy, respectively. Therefore, if GRB 190114C would have been fast located by HESS CT5 telescope, this burst would have been detected by HESS in accordance with our model. Similarly, bursts with similar features of GRB 190114C are perfect candidates for detection with future VHE facilities (e.g. CTA; Funk et al. 2013).

#### 3.3. The broadband Spectral Energy Distributions

The right-hand panels of Fig. 4 show the SEDs at 66 - 92 s (top panel) and 0.2 days (bottom panel). The synchrotron and SSC curves in a stratified (above) and homogeneous (below) medium were derived using the best-fit parameters reported in Fraija et al. (2019c). The EBL model introduced in Franceschini & Rodighiero (2017) was used. Radio, optical, X-ray, GBM and LAT data were taken from Laskar et al. (2019); Fraija et al. (2019c); Ravasio et al. (2019). The top panel shows that synchrotron emission describes the optical to LAT energy range and SSC emission contributes significantly to the LAT observations. The bottom panel shows that synchrotron emission explains the ratio to X-ray

data points. The flux ratio at the peaks are  $F_{\nu}^{\text{syn}}/F_{\nu}^{\text{SSC}} \simeq 10$  and  $\simeq 1$  at 66 - 90 s and 0.2 days, respectively. The SEDs can be explained through the evolution of synchrotron and SSC emissions in the stratified and the homogeneous medium. The decay of SSC emission is steeper than synchrotron radiation; in the stratified medium the decay of SSC and synchrotron evolve as  $\propto t^{-2.30}$  and  $\propto t^{-1.47}$ , respectively, and in the homogeneous medium as  $\propto t^{-1.21}$  and  $t^{-0.97}$ , respectively.

### 3.4. Why GRB 190114C is special in comparison to other LAT-detected bursts

The VHE flux above  $\sim 100$  GeV begins to be attenuated by pair production with EBL photons (Gould & Schröder 1966). The SSC flux observed is attenuated by  $\exp[-\tau_{\gamma\gamma}(z)]$  with  $\tau_{\gamma\gamma}(z)$  the photon-photon opacity as a function of redshift. Using the values of the opacities reported in Franceschini & Rodighiero (2017), VHE emission with photons at 300 GeV (1 TeV) is attenuated by 0.15 ( $2.1 \times 10^{-3}$ ) and  $6.6 \times 10^{-3}$  ( $2.2 \times 10^{-6}$ ) for  $z=0.5$  and 1, respectively. In the particular case of GRB 190114C, a low-redshift of  $z=0.42$  allowed the detection by an Imaging Atmospheric Cherenkov Telescope such as MAGIC.

We show that changes in density of the circumburst medium leads to an increase in the SSC emission. The afterglow transition reported in GRB 190114C allowed for enhanced VHE emission increased and hence was detected for a longer period.

The set of the best-fit parameters as reported for GRB 190114C made more favorable its detection by the MAGIC telescopes. As follows, we enumerate each one:

1. The SSC emission peaked below the KN regime, otherwise it would be drastically attenuated.
2. The peak of the SSC emission was reproduced at hundreds of GeVs, where MAGIC is more sensitive and the attenuation by EBL is small. Other configurations of parameters lead to peaks at few TeVs where the EBL absorption is much higher and therefore more difficult to detect by Imaging Atmospheric Cherenkov Telescopes (IACTs).
3. With the parameters given, the SSC flux evolved in the second PL segment of slow-cooling regime. In this case, we show that the SSC flux increases as the densities in both the stratified and homogeneous media increase. The values of densities in both cases make the detection of VHE flux more favorable.
4. The LAT light curve of GRB 190114C exhibited similar characteristics to other powerful bursts detected by Fermi LAT (see Fraija et al. 2019c).<sup>7</sup> These authors showed that GRB 190114C corresponded to one of the more powerful bursts during the first hundreds of seconds (early afterglow). In this work we show that higher values of the equivalent kinetic energy make the

SSC emission more favorable to be detected. Therefore, the total energy reported of this burst favored to its detection.

Notwithstanding attempts to detect the VHE emission at hundreds of GeVs by IACTs have been an arduous task because the time needed to locate the burst is longer than the duration of the prompt and early-afterglow emission, only one detection has been reported (GRB 190114C; Mirzoyan 2019). During the last two decades, only upper VHE limits have been derived by these telescopes (e.g. see, Albert et al. 2007; Aleksić et al. 2014; Aharonian et al. 2009a,b; H.E.S.S. Collaboration et al. 2014; Acciari et al. 2011; Bartoli et al. 2017; Abeyssekara et al. 2018). We conclude that the conditions to locate promptly the early afterglow of GRB 190114C by the MAGIC telescope together with the low-redshift and favorable set of parameters made its detection possible. We want to highlight that no other LAT-detected burst complies with all the requirements mentioned above. It is worth noting that although GRB 130427A was closer and more energetic than GRB 190114C (Ackermann et al. 2014), it was not located rapidly enough to catch the early afterglow by IACTs.<sup>8</sup>

## 4. CONCLUSIONS

We have computed the SSC light curves for a stratified stellar-wind that transitions to an homogeneous ISM-like medium, taking into account the synchrotron forward-shock models introduced in Sari et al. (1998), Chevalier & Li (2000) and Panaitescu & Kumar (2000). The break energy in the KN regime was obtained. The attenuation produced by the EBL absorption is introduced in accordance with the model presented in Franceschini & Rodighiero (2017). The intrinsic attenuation by  $e^{\pm}$  pair production (opacity) is not taken into account because during the deceleration phase it is much less than unity ( $\tau_{\gamma\gamma,\text{in}} \ll 1$ ).

In general, we compute the SSC light curves for a stratified and homogeneous medium at 10 and 100 GeV and compare them with the LAT and MAGIC sensitivities. We show that depending on the parameter values, the SSC light curves are above the LAT and MAGIC sensitivities. We calculate the SSC light curves during the afterglow transition and show that for this transition to be well-identified, it is necessary not only to observe the synchrotron, but also the SSC emission. For instance, the SSC emission can help us to discriminate between the stratified-to-homogeneous afterglow transition and a reverse-shock scenario. We have computed the SED in the stratified and homogeneous medium and also discussed their differences.

We emphasize that the equations of synchrotron flux are degenerate in parameters such that for an entirely distinct set of parameters same results can be obtained. Therefore, this result is not unique, but it is a possible solution for GRB 190114C. It is worth noting that if the increase of the observed SSC flux around  $\sim 400$  s is not exhibited, then other set of parameters to describe GRB 190114C is required or an alternative scenario would have to be evoked.

Using the best-fit parameters reported for GRB 190114C, we have estimated the SSC light curves and fitted the SEDs for two epochs 66 - 92 s and 0.2 days. We show that SSC process could explain the VHE photons beyond the synchrotron limit in GRB 190114C.

<sup>7</sup> GRB 080916C, GRB 090510, GRB 090902B, GRB 090926A, GRB 110721A, GRB 110731A, GRB 130427A and GRB 160625B and others (Abdo et al. 2009b; Ackermann & et al. 2010; Abdo et al. 2009a; Ackermann et al. 2011; Ackermann & et al. 2013; Fraija et al. 2017a; Ackermann & et al. 2013; Ackermann et al. 2014; Fraija et al. 2017b)

<sup>8</sup> VERITAS started follow-up observations of GRB 130427A  $\sim 20$  hours after the trigger time (Aliu et al. 2014).



Recently, Wang et al. (2019a) described the broadband SED of GRB 190114C with a SSC model for a homogeneous medium using the optical, X-ray and LAT data between 50 - 150 s. They concluded that the detection of sub-TeV photons is attributed to the large burst energy and low redshift. Derishev & Piran (2019) studied the physical conditions of the afterglow required for explaining the sub-TeV photons in GRB 190114C. These authors found that the Comptonization of X-ray photons at the border between Thompson and KN regime with a bulk and electron Lorentz factor of  $\simeq 100$  and  $\gamma_c \simeq 10^4$  could described the MAGIC detection. In our current work, in addition to study the evolution of SSC light curves during the stratified-to-homogeneous afterglow transition as reported in Fraija et al. (2019c), we have interpreted the photons beyond the synchrotron limit in the SSC framework and hence model its SED in the stratified and the homogeneous medium. We conclude that although the photons beyond the synchrotron limit can be interpreted by SSC process, the emission detected at hundreds of GeVs is due to the closeness and the set of favorable parameter values

of this burst. We conclude that low-redshift GRBs described under favourable set of parameters as found in GRB 190114C could be detected at hundreds of GeVs, and also afterglow transitions would allow that VHE emission could be observed for longer periods. The results of our afterglow model in the homogeneous medium is consistent with the results reported in Derishev & Piran (2019). In our case, the SSC emission is below the KN regime 868.1 GeV with a bulk and electron Lorentz factors of 101.2 and  $1.9 \times 10^{-4}$ , respectively. It is worth noting that the parameters obtained with the MCMC code from the broadband modeling of the multi-wavelength observations may change somewhat when the KN effects are considered, but the SSC emission itself will not be strongly affected.

We thank Xiang-Yu Wang and B.B Zhang for useful discussions. N. F. acknowledge financial support from UNAM-DGAPA-PAPIIT through Grant IA 102019. RBD acknowledges support from the National Science Foundation under Grant 1816694.

## REFERENCES

- Aartsen, M. G., Ackermann, M., Adams, J., et al. 2015, *ApJ*, 805, L5  
Aartsen, M. G., Abraham, K., Ackermann, M., et al. 2016, *ApJ*, 824, 115  
Abbasi, R., Abdou, Y., Abu-Zayyad, T., et al. 2012, *Nature*, 484, 351  
Abdo, A. A., Ackermann, M., Ajello, M., et al. 2009a, *ApJ*, 706, L138  
Abdo, A. A., Ackermann, M., Arimoto, M., et al. 2009b, *Science*, 323, 1688  
Abeyssekara, A. U., Archer, A., Benbow, W., et al. 2018, *ArXiv e-prints*, arXiv:1803.01266  
Abeyssekara, A. U., & et al. 2012, *Astroparticle Physics*, 35, 641  
Acciari, V. A., Aliu, E., Arlen, T., et al. 2011, *ApJ*, 743, 62  
Ackermann, M., & et al. 2010, *ApJ*, 716, 1178  
—, 2013, *ApJ*, 763, 71  
Ackermann, M., Ajello, M., Asano, K., et al. 2011, *ApJ*, 729, 114  
—, 2013, *ApJS*, 209, 11  
—, 2014, *Science*, 343, 42  
Aharonian, F., Akhperjanian, A. G., Barres de Almeida, U., et al. 2009a, *A&A*, 495, 505  
Aharonian, F., Akhperjanian, A. G., Barres DeAlmeida, U., et al. 2009b, *ApJ*, 690, 1068  
Ajello, M., Arimoto, M., Axelsson, M., et al. 2019, *The Astrophysical Journal*, 878, 52  
Albert, J., Aliu, E., Anderhub, H., et al. 2007, *ApJ*, 667, 358  
Aleksić, J., Ansoldi, S., Antonelli, L. A., et al. 2014, *MNRAS*, 437, 3103  
Alexander, K. D. e. a. 2019, *GRB Coordinates Network, Circular Service*, No. 23726, 23726  
Aliu, E., Aune, T., Barnacka, A., et al. 2014, *ApJ*, 795, L3  
Asano, K., Guiriec, S., & Mészáros, P. 2009, *ApJ*, 705, L191  
Barniol Duran, R., & Kumar, P. 2011, *MNRAS*, 412, 522  
Bartoli, B., Bernardini, P., Bi, X. J., et al. 2017, *ApJ*, 842, 31  
Beniamini, P., Nava, L., Duran, R. B., & Piran, T. 2015, *MNRAS*, 454, 1073  
Beniamini, P., Nava, L., & Piran, T. 2016, *MNRAS*, 461, 51  
Beniamini, P., & van der Horst, A. J. 2017, *MNRAS*, 472, 3161  
Bolmer, J., & Shady, P. 2019, *GRB Coordinates Network, Circular Service*, No. 23702, 23702  
Chevalier, R. A., & Li, Z.-Y. 2000, *ApJ*, 536, 195  
Chevalier, R. A., Li, Z.-Y., & Fransson, C. 2004, *ApJ*, 606, 369  
Dai, Z. G., & Lu, T. 1998, *MNRAS*, 298, 87  
D’Avanzo, P. e. a. 2019, *GRB Coordinates Network, Circular Service*, No. 23729, 23729  
Derishev, E., & Piran, T. 2019, *arXiv e-prints*, arXiv:1905.08285  
Dermer, C. D., Böttcher, M., & Chiang, J. 2000, *ApJ*, 537, 255  
Fraija, N. 2014, *MNRAS*, 437, 2187  
Fraija, N., De Colle, F., Veres, P., et al. 2019a, *ApJ*, 871, 123  
—, 2019b, *arXiv e-prints*, arXiv:1906.00502  
Fraija, N., Dichiarà, S., Pedreira, A. C. C. d. E. S., et al. 2019c, *ApJ*, 879, L26  
Fraija, N., González, M. M., & Lee, W. H. 2012, *ApJ*, 751, 33  
Fraija, N., Lee, W., & Veres, P. 2016a, *ApJ*, 818, 190  
Fraija, N., Lee, W. H., Araya, M., et al. 2017a, *ApJ*, 848, 94  
Fraija, N., Lee, W. H., Veres, P., & Barniol Duran, R. 2016b, *ApJ*, 831, 22  
Fraija, N., Lopez-Camara, D., Pedreira, A. C. C. d. E. S., et al. 2019d, *arXiv e-prints*, arXiv:1904.07732  
Fraija, N., Pedreira, A. C. C. d. E. S., & Veres, P. 2019e, *ApJ*, 871, 200  
Fraija, N., & Veres, P. 2018, *ApJ*, 859, 70  
Fraija, N., Veres, P., Zhang, B. B., et al. 2017b, *ApJ*, 848, 15  
Fraija, N., Dichiarà, S., Pedreira, A. C. C. d. E. S., et al. 2019f, *arXiv e-prints*, arXiv:1905.13572  
Franceschini, A., & Rodighiero, G. 2017, *A&A*, 603, A34  
Frederiks, D., Golenetskii, S., Aptekar, R., et al. 2019, *GRB Coordinates Network, Circular Service*, No. 23737, #1 (2019), 23737  
Funk, S., & Hinton, J. 2013, *Astroparticle Physics*, 43, 348, seeing the High-Energy Universe with the Cherenkov Telescope Array - The Science Explored with the CTA  
Funk, S., Hinton, J. A., & CTA Consortium. 2013, *Astroparticle Physics*, 43, 348  
Ghisellini, G., Ghirlanda, G., Nava, L., & Celotti, A. 2010, *MNRAS*, 403, 926  
Gould, R. J., & Schröder, G. 1966, *Phys. Rev. Lett.*, 16, 252  
Gropp, J. D. e. a. 2019, *GRB Coordinates Network, Circular Service*, No. 23688, 23688  
H.E.S.S. Collaboration, Abramowski, A., Aharonian, F., et al. 2014, *A&A*, 565, A16  
Hurley, K., Dingus, B. L., Mukherjee, R., et al. 1994, *Nature*, 372, 652  
Im, M. e. a. 2019a, *GRB Coordinates Network, Circular Service*, No. 23717, 23717  
—, 2019b, *GRB Coordinates Network, Circular Service*, No. 23740, 23740  
Izzo, L. e. a. 2019, *GRB Coordinates Network, Circular Service*, No. 23699, 23699  
Kobayashi, S. 2000, *ApJ*, 545, 807  
Kocevski, D. e. a. 2019, *GRB Coordinates Network, Circular Service*, No. 23709, 23709  
Kumar, P., & Barniol Duran, R. 2009, *MNRAS*, 400, L75  
—, 2010, *MNRAS*, 409, 226  
Laskar, T., Alexander, K. D., Gill, R., et al. 2019, *arXiv e-prints*, arXiv:1904.07261  
Lipunov, V. e. a. 2019, *GRB Coordinates Network, Circular Service*, No. 23693, 23693  
Liu, R.-Y., Wang, X.-Y., & Wu, X.-F. 2013, *ApJ*, 773, L20  
Longo, F., Bissaldi, E., Vianello, G., et al. 2016, *GRB Coordinates Network, Circular Service*, No. 19413, #1 (2016), 19413  
Mazaeva, E. e. a. 2019, *GRB Coordinates Network, Circular Service*, No. 23741, 23741  
Mészáros, P., & Rees, M. J. 2000, *ApJ*, 541, L5  
Minaev, P., & Pozanenko, A. 2019, *GRB Coordinates Network, Circular Service*, No. 23714, #1 (2019), 23714  
Mirzoyan, R. e. a. 2019, *GRB Coordinates Network, Circular Service*, No. 23701, 23701  
Nakar, E., Ando, S., & Sari, R. 2009, *ApJ*, 703, 675  
Nava, L., Vianello, G., Omodei, N., et al. 2014, *MNRAS*, 443, 3578

- Osborne, J. P. e. a. 2019, GRB Coordinates Network, Circular Service, No. 23704, 23704
- Panaitescu, A., & Kumar, P. 2000, *ApJ*, 543, 66
- Panaitescu, A., & Mészáros, P. 2000, *ApJ*, 544, L17
- Panaitescu, A., Vestrand, W. T., & Woźniak, P. 2014, *ApJ*, 788, 70
- Papathanassiou, H., & Meszaros, P. 1996, *ApJ*, 471, L91
- Piran, T., & Nakar, E. 2010, *ApJ*, 718, L63
- Piron, F. 2016, *Comptes Rendus Physique*, 17, 617
- Planck Collaboration, Aghanim, N., Akrami, Y., et al. 2018, arXiv e-prints, arXiv:1807.06209
- Ravasio, M. E., Oganessyan, G., Salafia, O. S., et al. 2019, arXiv e-prints, arXiv:1902.01861
- Sacahui, J. R., Fraija, N., González, M. M., & Lee, W. H. 2012, *ApJ*, 755, 127
- Santana, R., Barniol Duran, R., & Kumar, P. 2014, *ApJ*, 785, 29
- Sari, R., & Esin, A. A. 2001, *ApJ*, 548, 787
- Sari, R., Piran, T., & Narayan, R. 1998, *ApJ*, 497, L17
- Selsing, J. e. a. 2019, GRB Coordinates Network, Circular Service, No. 23695, 23695
- Siegel, M. H. e. a. 2019, GRB Coordinates Network, Circular Service, No. 23725, 23725
- Takahashi, K., Murase, K., Ichiki, K., Inoue, S., & Nagataki, S. 2008, *ApJ*, 687, L5
- Tyurina, N. e. a. 2019, GRB Coordinates Network, Circular Service, No. 23690, 23690
- Ugarte Postigo, A. e. a. 2019, GRB Coordinates Network, Circular Service, No. 23692, 23692
- Ursi, A., Tavani, M., Marisaldi, M., et al. 2019, GRB Coordinates Network, Circular Service, No. 23712, #1 (2019), 23712
- Vandenbroucke, J. 2019, *The Astronomer's Telegram*, 12395, 1
- Vedrenne, G., & Atteia, J.-L. 2009, *Gamma-Ray Bursts*, doi:10.1007/978-3-540-39088-6
- Veres, P., & Mészáros, P. 2012, *ApJ*, 755, 12
- Vink, J. S., & de Koter, A. 2005, *A&A*, 442, 587
- Vink, J. S., de Koter, A., & Lamers, H. J. G. L. M. 2000, *A&A*, 362, 295
- Wang, X. Y., Dai, Z. G., & Lu, T. 2001, *ApJ*, 546, L33
- Wang, X.-Y., He, H.-N., Li, Z., Wu, X.-F., & Dai, Z.-G. 2010, *ApJ*, 712, 1232
- Wang, X.-Y., Liu, R.-Y., & Lemoine, M. 2013, *ApJ*, 771, L33
- Wang, X.-Y., Liu, R.-Y., Zhang, H.-M., Xi, S.-Q., & Zhang, B. 2019a, arXiv e-prints, arXiv:1905.11312
- Wang, Y., Li, L., Moradi, R., & Ruffini, R. 2019b, arXiv e-prints, arXiv:1901.07505
- Xiao, S., Li, C. K., Li, X. B., et al. 2019, GRB Coordinates Network, Circular Service, No. 23716, #1 (2019), 23716
- Zhang, B., & Mészáros, P. 2001, *ApJ*, 559, 110
- Zou, Y.-C., Fan, Y.-Z., & Piran, T. 2009, *MNRAS*, 396, 1163

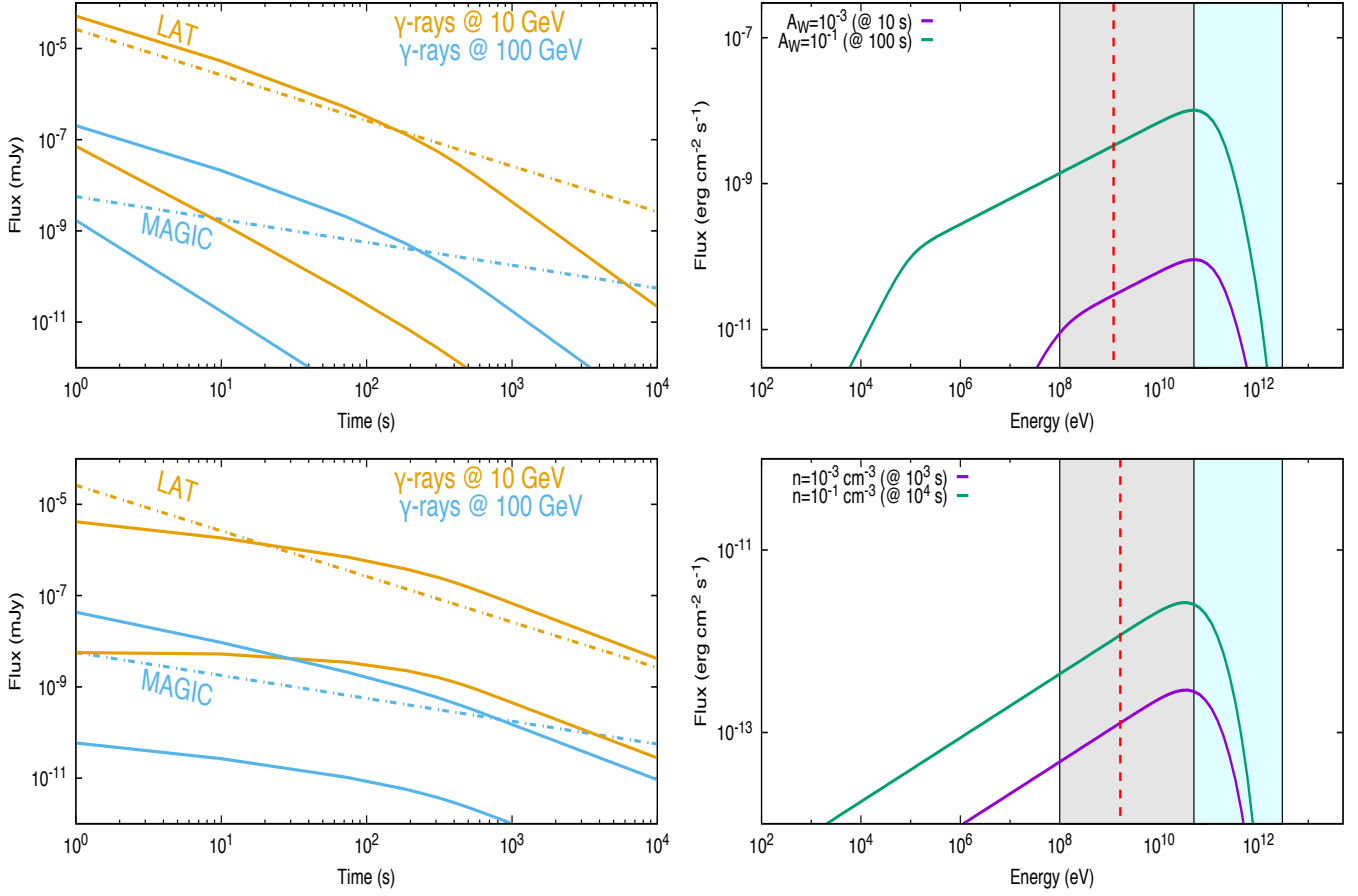


FIG. 1.— The figures show the light curves (left) and SEDs (right) of SSC emission expected from a decelerating outflow in a stratified (above) and homogeneous (below) medium for values of  $A_W = 10^{-3}$  ( $10^{-1}$ ) and  $n = 10^{-3}$  ( $10^{-1}$ )  $\text{cm}^{-3}$ , respectively. In all panels the values of  $E = 5 \times 10^{53}$  erg,  $p = 2.3$ ,  $\epsilon_B = 10^{-3}$ ,  $\epsilon_e = 10^{-2}$  and  $z = 0.5$  were used. Dashed-dotted lines in left panels represent the LAT (gold; [Piron 2016](#)) and MAGIC (blue; [Takahashi et al. 2008](#)) sensitivities at 10 and 100 GeV respectively. The light curves above the LAT and MAGIC sensitivities are obtained with  $A_W = 10^{-1}$  and  $n = 10^{-1} \text{ cm}^{-3}$  for a stratified and homogeneous medium and below the sensitivities are obtained with  $A_W = 10^{-3}$  and  $n = 10^{-3} \text{ cm}^{-3}$ , respectively. The SEDs are shown at two different times,  $t = 10$  and  $100$  s for the wind medium, and  $t = 10^3$  and  $10^4$  s for the homogeneous medium. The red dashed lines correspond to the synchrotron limit. The filled areas in gray and cyan colors correspond to the Fermi LAT and MAGIC energy ranges, respectively. The effect of the extragalactic background light (EBL) absorption proposed by [Franceschini & Rodighiero \(2017\)](#).



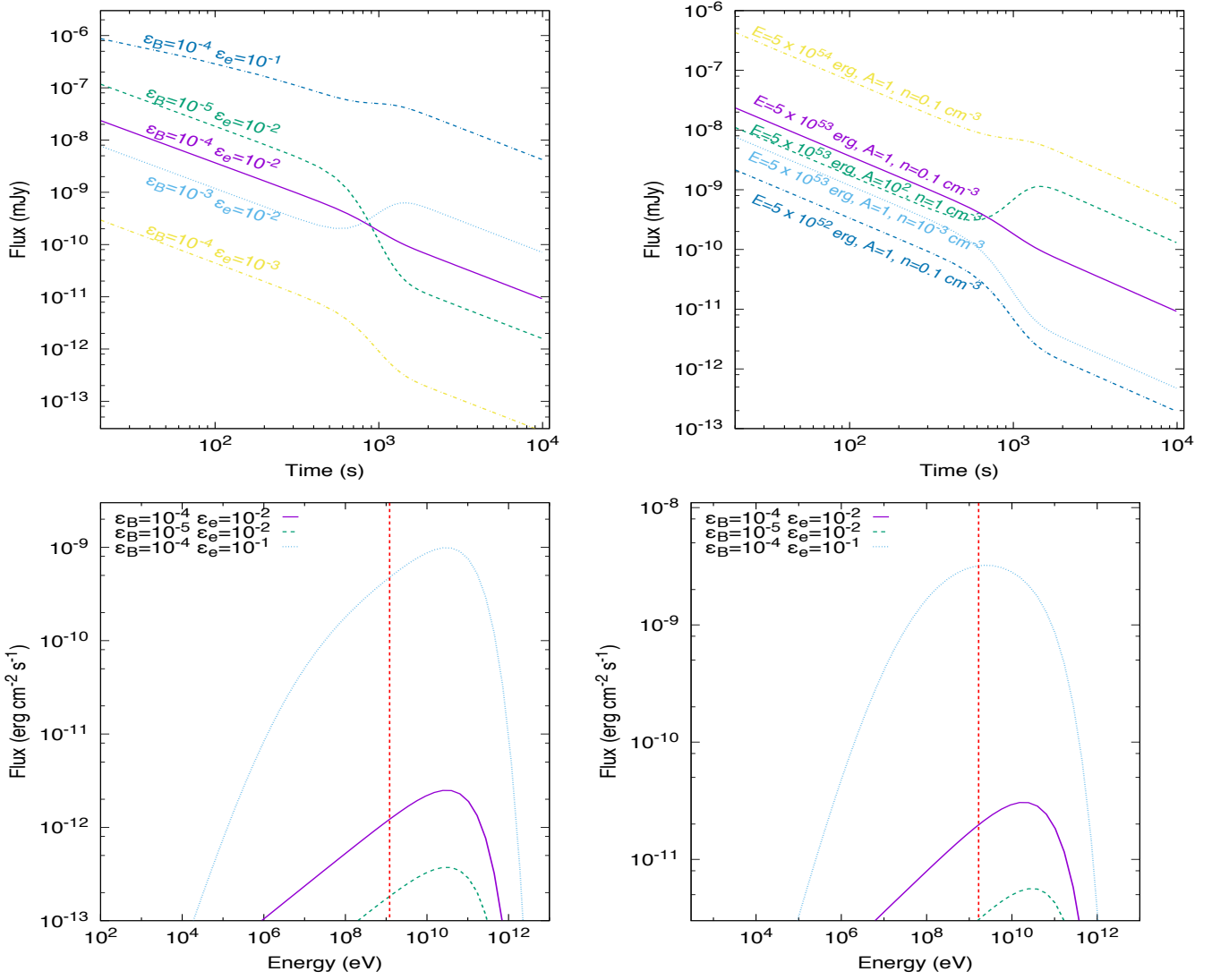


FIG. 2.— Figure shows the SSC light curves and spectra during the afterglow transition between the stratified and homogeneous medium (considered here at 1000 s) for relevant values of GRB afterglows. In the top left-hand panel, light curves are obtained for  $E = 5 \times 10^{53}$  erg,  $A_w = 1$  and  $n = 1 \text{ cm}^{-3}$ , and in the top right-hand panel these are for  $\varepsilon_B = 10^{-4}$  and  $\varepsilon_B = 10^{-2}$ . The Top panels show the SSC light curves for  $\epsilon_\gamma = 100 \text{ GeV}$  and the bottom ones the SSC spectra computed in the stratified (left) and homogeneous (right) medium. The SSC spectra in the stratified medium are computed for  $t = 900 \text{ s}$  and in the homogeneous medium for  $t = 1100 \text{ s}$ . The red dashed line corresponds to the maximum energy radiated by synchrotron.

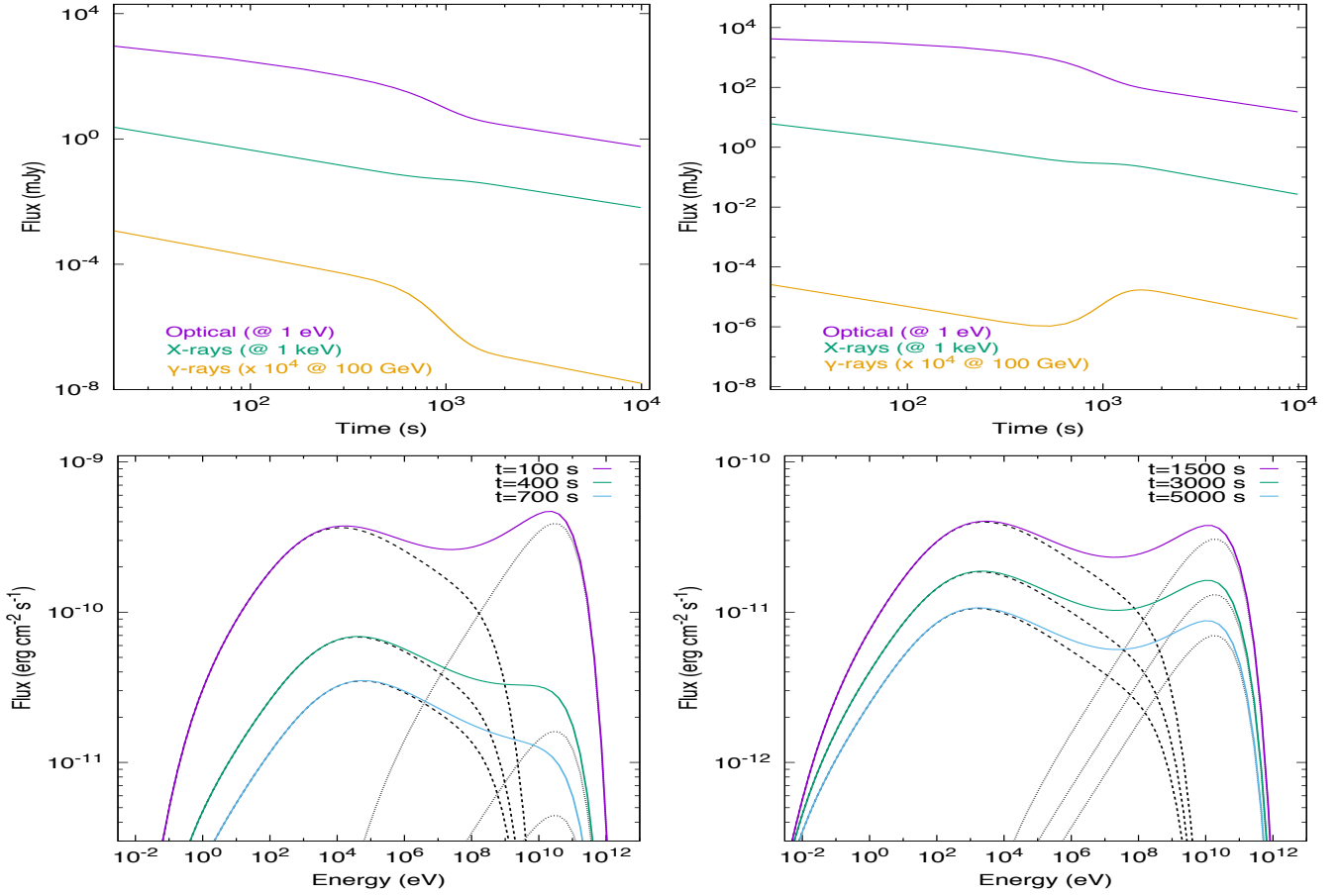


FIG. 3.— Figure shows the SSC and synchrotron light curves (SSC model) and the broadband SEDs during the afterglow transition between the stratified and homogeneous medium. The top panels show the synchrotron light curves of optical and X-ray bands at 1 eV and 1 keV, and the SSC light curves of  $\gamma$ -rays at 100 GeV. In the top left-hand panel, the light curves are computed for  $E = 5 \times 10^{53}$  erg,  $A_w = 0.1$ ,  $n = 0.1 \text{ cm}^{-3}$ ,  $\varepsilon_B = 10^{-4}$ ,  $\varepsilon_e = 10^{-2}$  and  $\xi = 1$ , and in the top right-hand panel, these are obtained for  $E = 10^{54}$  erg,  $A_w = 1$ ,  $n = 1 \text{ cm}^{-3}$ ,  $\varepsilon_B = 10^{-3}$ ,  $\varepsilon_e = 10^{-2}$  and  $\xi = 0.5$ . The bottom panels show the broadband SEDs (both synchrotron - dashed, and SSC - dotted) computed in the stratified medium for  $t = 100, 400$  and  $700$  s (left) and the homogeneous medium for  $t = 1500, 3000$  and  $5000$  s (right). The stratified-to-homogeneous transition is considered at 1000 s, as in Fig. 2. In the bottom panels, the SEDs are computed for  $E = 5 \times 10^{53}$  erg,  $\varepsilon_B = 10^{-4}$  and  $\varepsilon_e = 10^{-2}$ , with the densities of  $A_w = 0.1$  (left) and  $n = 1 \text{ cm}^{-3}$  (right).

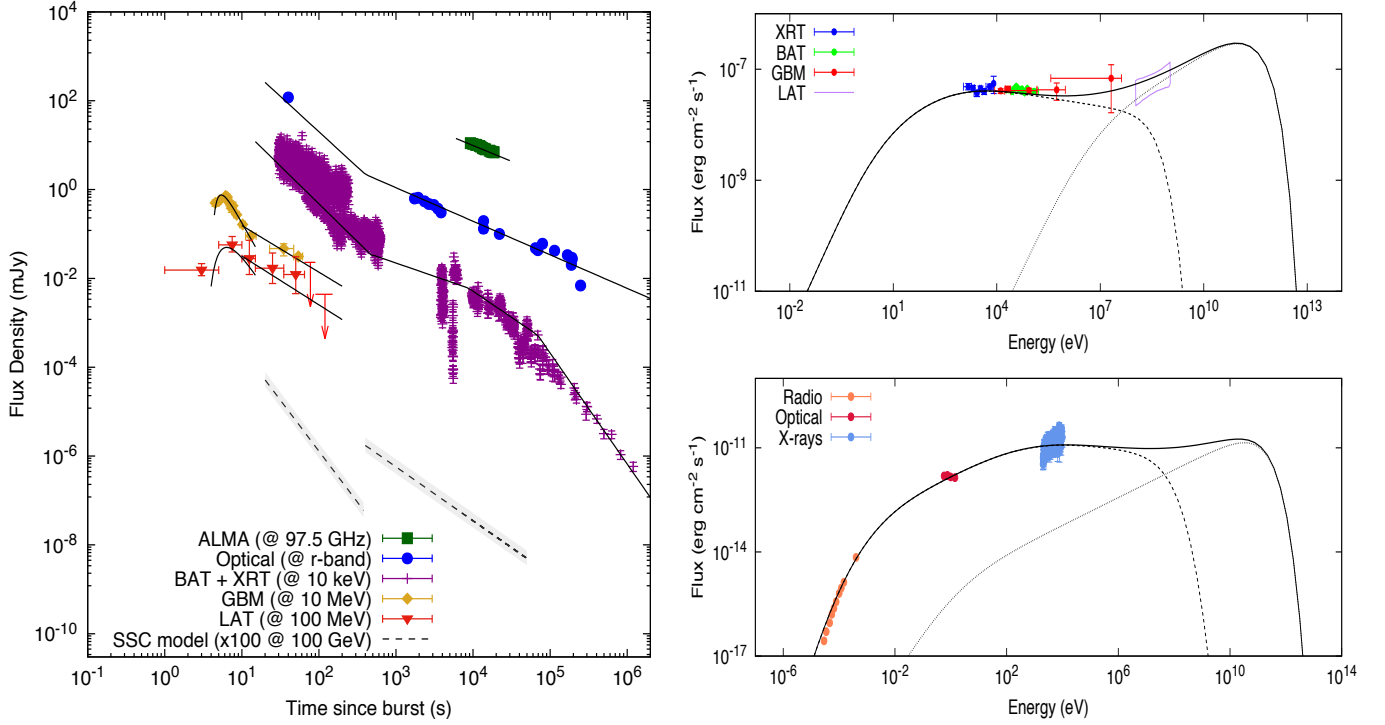


FIG. 4.— The SSC light curves (left) and SEDs (right) of GRB 190114C are shown. The synchrotron and SSC curves in a stratified and homogeneous medium were derived using the best-fit parameters reported in [Fraija et al. \(2019c\)](#). The broadband SEDs are built from two time intervals 66 - 92 s (above) and 0.2 days (below). The left-hand panel is adapted from [Fraija et al. \(2019c\)](#). The effect of the extragalactic background light (EBL) absorption proposed by [Franceschini & Rodighiero \(2017\)](#) is taken into account. Radio, optical, X-ray, GBM and LAT data were taken from [Laskar et al. \(2019\)](#); [Fraija et al. \(2019c\)](#); [Ravasio et al. \(2019\)](#). The values used to obtain the SSC light curves and SEDs are  $A_W = 6 \times 10^{-2}$ ,  $n = 1 \text{ cm}^{-3}$ ,  $E = 2 \times 10^{54} \text{ erg}$ ,  $\varepsilon_B = 5 \times 10^{-6}$ ,  $\varepsilon_e = 10^{-2}$  and  $p = 2.3$  ([Fraija et al. 2019c](#)).



## APPENDIX

The proportionality constants in the stratified medium, eq. (4), are

$$\begin{aligned}
F_{1,f}^W &\simeq 2.3 \times 10^{-5} \text{ mJy} \left( \frac{1+Y_{\text{Th}}}{3} \right)^{\frac{4}{3}} \left( \frac{1+z}{1.5} \right)^3 \xi^4 \varepsilon_{\text{B},-4}^{\frac{5}{3}} A_{W,-1}^{-4} D_{27}^{-2} E_{53.5}^{-\frac{1}{3}}, \\
F_{2,f}^W &\simeq 2.1 \times 10^{-3} \text{ mJy} \left( \frac{1+Y_{\text{Th}}}{3} \right)^{-2} \left( \frac{1+z}{1.5} \right)^{\frac{1}{2}} \xi^{-\frac{1}{4}} \varepsilon_{\text{B},-4}^{-\frac{5}{4}} D_{27}^{-2} A_{W,-1}^{\frac{1}{4}} E_{53.5}^{\frac{1}{2}}, \\
F_{3,f}^W &\simeq 2.5 \times 10^{-7} \text{ mJy} g(p)^{2(p-1)} \left( \frac{1+Y_{\text{Th}}}{3} \right)^{-2} \left( \frac{1+z}{1.5} \right)^{\frac{p}{2}} \xi^{\frac{p-2}{4}} \varepsilon_{\text{B},-4}^{\frac{p-6}{4}} \varepsilon_{e,-2}^{2(p-1)} A_{W,-1}^{\frac{2-p}{4}} D_{27}^{-2} E_{53.5}^{\frac{p}{2}}, \\
F_{1,s}^W &\simeq 4.2 \times 10^{-2} \text{ mJy} g(p)^{-\frac{4}{3}} \left( \frac{1+z}{1.5} \right)^{\frac{5}{3}} \xi^{-\frac{8}{3}} \varepsilon_{\text{B},-4}^{\frac{1}{3}} \varepsilon_{e,-2}^{-\frac{4}{3}} A_{W,-1}^{\frac{8}{3}} D_{27}^{-2} E_{53.5}^{-\frac{1}{3}}, \\
F_{2,s}^W &\simeq 8.6 \times 10^{-10} \text{ mJy} g(p)^{2(p-1)} \left( \frac{1+z}{1.5} \right)^{\frac{p+3}{2}} \xi^{\frac{p-11}{4}} \varepsilon_{\text{B},-4}^{\frac{p+1}{4}} \varepsilon_{e,-2}^{2(p-1)} A_{W,-1}^{\frac{11-p}{4}} D_{27}^{-2} E_{53.5}^{\frac{p-1}{2}},
\end{aligned}$$

with  $F_{3,s}^W = F_{3,f}^W$ . The proportionality constants in the homogeneous medium, eq. (10), are

$$\begin{aligned}
F_{1,f}^H &\simeq 2.3 \times 10^{-5} \text{ mJy} \left( \frac{1+Y_{\text{Th}}}{2.5} \right)^{\frac{4}{3}} \varepsilon_{\text{B},-4}^{\frac{5}{3}} n^{-2} D_{27}^{-2} E_{53.5}^{\frac{5}{3}}, \\
F_{2,f}^H &\simeq 2.5 \times 10^{-6} \text{ mJy} \left( \frac{1+Y_{\text{Th}}}{2.5} \right)^{-2} \left( \frac{1+z}{1.5} \right)^{\frac{3}{8}} \varepsilon_{\text{B},-4}^{-\frac{5}{4}} D_{27}^{-2} n^{\frac{1}{8}} E_{53.5}^{\frac{5}{8}}, \\
F_{3,f}^H &\simeq 2.7 \times 10^{-10} \text{ mJy} g(p)^{2(1-p)} \left( \frac{1+Y_{\text{Th}}}{2.5} \right)^{-2} \left( \frac{1+z}{1.5} \right)^{\frac{5p-2}{8}} \varepsilon_{\text{B},-4}^{\frac{p-6}{8}} \varepsilon_{e,-2}^{2p-2} D_{27}^{-2} E_{53.5}^{\frac{3p+2}{8}}, \\
F_{1,s}^H &\simeq 4.6 \times 10^{-3} \text{ mJy} g(p)^{\frac{4}{3}} \left( \frac{1+z}{1.5} \right)^{\frac{1}{3}} \varepsilon_{\text{B},-4}^{\frac{1}{3}} \varepsilon_{e,-2}^{-\frac{4}{3}} n^{\frac{4}{3}} D_{27}^{-2} E_{53.5}, \\
F_{2,s}^H &\simeq 7.4 \times 10^{-11} \text{ mJy} g(p)^{2(p-1)} \left( \frac{1+z}{1.5} \right)^{\frac{5p+1}{8}} \varepsilon_{\text{B},-4}^{\frac{p+1}{4}} \varepsilon_{e,-2}^{2(p-1)} n^{\frac{11-p}{8}} D_{27}^{-2} E_{53.5}^{\frac{3p+7}{8}},
\end{aligned}$$

with  $F_{3,s}^H = F_{3,f}^H$ .